2.12.3 aClimax

The software package aClimax was used to calculate INS spectra from the results of CASTEP phonon calculations.[93] It is possible to do this because the intensity of the INS signal is directly proportional to the amplitude of motion and the scattering cross sections of the atoms involved. The program was also used to calculate Raman spectra. Calculated spectra shown in this Thesis include the primary modes, and 1–2, 0–2, 0–3, and 0–4 overtones.

2.13 Phase Transitions[94]

The IGA$^{\mathrm{n}}$ and low temperature in-situ diffraction techniques used in this Thesis are very powerful techniques for observing phase transitions. In the solid state, there are three main types of phase transition, they are *i*) first-order; *ii*) second-order; and *iii*) the γ-transition. The type of change can be identified using changes in thermodynamic parameters, and a scheme known as the Ehrenfest classification. Many phase changes are accompanied by changes in volume and enthalpy, these changes have implications for the slopes of the chemical potentials of the phases at either side of the phase transition. For a transition from a phase α to phase β,

$$\begin{aligned} \left(\frac{\partial \mu_\beta}{\partial p}\right)_T - \left(\frac{\partial \mu_\alpha}{\partial p}\right)_T &= V_{\beta,m} - V_{\alpha,m} = \Delta_{trs} V \\ \left(\frac{\partial \mu_\beta}{\partial T}\right)_p - \left(\frac{\partial \mu_\alpha}{\partial T}\right)_p &= -S_{\beta,m} + S_{\alpha,m} = -\Delta_{trs} S = -\frac{\Delta_{trs} H}{T_{trs}} \end{aligned} \tag{2.33}$$

When $\Delta_{trs}V$and $\Delta_{trs}H$ are non-zero, the slopes of the chemical potential plotted against either pressure or temperature are different either side of the transition. So the the first derivatives of the chemical potentials with respect to temperature or pressure are discontinuous at the transition. Transitions where the first derivative with respect to temperature is discontinuous are classified as first-order. For a second-order transition, the first derivative of the chemical potential with respect to temperature is continuous, but the second derivative is discontinuous. A γ-transition is not first-order, but is one where the heat capacity becomes infinite at the transition temperature (as it does for a first-order transition).

In crystallography, the volume changes associated with phase transitions are relatively easy to observe, for a first-order transition there will be a finite volume change at the transition, while for a second-order there will be no volume change at the transition. Second-order transitions are generally associated with a change in the symmetry of the crystal structure. An example of this is a tetragonal cell expanding faster along its two common directions than along the third, at a point when all the cell lengths are equal the cell will be cubic, and as all the directions are now equivalent, the cell will expand equally along them all. A phase transition has occurred, but there is no discontinuity in the volume so it is second-order.

Chapter 3

Lithium Borohydride Ammines

3.1 Introduction

This Chapter focuses on the structural solution of the lithium borohydride ammines: $Li(NH_3)_nBH_4$, with $n = 1, 2, 3$ and 4. The structural solution is based on X-ray and neutron diffraction, solution and solid state NMR, DFT calculations, and gravimetric analysis techniques. The themes of dihydrogen bonding and structural disorder are frequently addressed, and full structural solution for each phase is presented. Phase transformations are investigated from both experimental and theoretical results and the ammonia storage properties and potential of $LiBH_4$ are evaluated.

3.2 In-situ Experiments on GEM and HRPD

Isotopically enriched $Li^{11}BD_4$ was synthesised from the elements using the high pressure furnace and procedure described in Chapter 2 Section 2.3. The ammines, $Li(ND_3)_n^{11}BD_4$, were then produced in-situ using the IGA^n equipment (see Section 2.11.3) on the GEM and HRPD powder diffractometers at ISIS (described in Sections 2.7.1 and 2.7.2 respectively).

A summary of the initial experiment carried out on GEM is shown in Figure 3.1, where it can be seen that four crystalline phases exist with masses corresponding to n $= 1, 2, 3$ and 4. The starting sample of $Li(ND_3)_4^{11}BD_4$ was obtained by exposing $Li^{11}BD_4$ to ND_3 at a pressure of 1000 mbar for a period of 48 hours. By monitoring the diffraction data and the sample mass, it was possible to reduce the pressure incrementally until the pure phases were observed. The set point pressures used to isolate the phases with n = 3, 2, and 1 were 67 mbar, ca. 27 mbar and 3 mbar (with the IGA set to 'outgas') respectively, the room temperature during the experiment varied between 19 °C and 20 °C. It should be noted here that although Figure 3.1 represents real time data collection, various sections have been cut from the data to improve clarity. These include a section when the n = 2 phase turned amorphous and a pressure increase leading to conversion from the n = 3 to the n = 4 phase. Ideally these data would be of sufficient quality for structure solution however as Figures 3.1 and 3.2 show, intense steel reflections are present in the data. There is also significant overlap of $Li(ND_3)_n^{11}BD_4$ reflections as shown in Figure 3.2. The combination of these factors is enough to require more diffraction data with greater resolution and ideally no steel reflections. However the useful conclusion remains that 4 distinct crystalline phases exist.

The investigation was furthered using HRPD and the quartz tail of the IGA^n reactor which was used for the first time in this experiment, the sample mass and ND_3 pressure data from this experiment are shown in Figure 3.3. Once again, the starting $Li(ND_3)_4^{11}BD_4$ sample was obtained by exposing $Li^{11}BD_4$ to ND_3 at a pressure of 1000 mbar, but for a period of 12 hours. Transitions to phases n = 3, 2 and 1 were isobaric occurring at a room temperature of between 21 °C and 23 °C, and observed at set-point ammonia vapour pressures of 67 mbar, ca. 24 mbar, and 0 mbar (with the IGA set to 'outgas') respectively. The result of using the quartz tail was an increased (quartz) background intensity but a massively reduced appearance of steel reflections. The steel reflections still present are produced by the heating element of the IGA^n, as discussed in Section 2.11.3. Crystalline phases

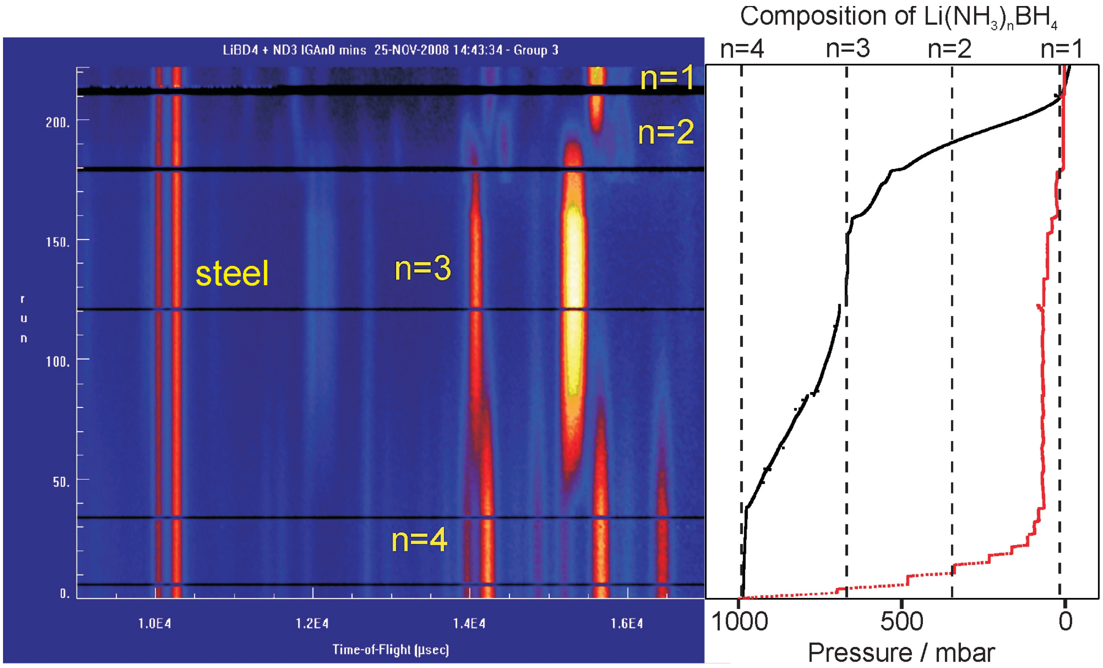

Figure 3.1: A summary of the IGA^n experiment on GEM, showing diffraction data collected using bank 4 on the left hand side (most intense peaks are yellow, background is blue) with sample mass (black) and ND_3 pressure (red) on the right hand side.

were identified for n = 1, 3 and 4, and diffraction data for the n = 3 and 4 phases were collected for several beam hours using both of the HRPD chopper settings in order to collect high resolution data over the widest possible range of d-spacings. Data collected at each chopper setting were then normalised and merged into a single set of diffraction data covering the widest possible range of time of flight. These merged data were used for the structural solution discussed in the following Sections. Despite the mass trace showing a plateau at n = 2, no Bragg reflections were observed in the diffraction data collected during this period, suggesting that the n = 2 phase was present as a liquid as it was for part of the GEM experiment.

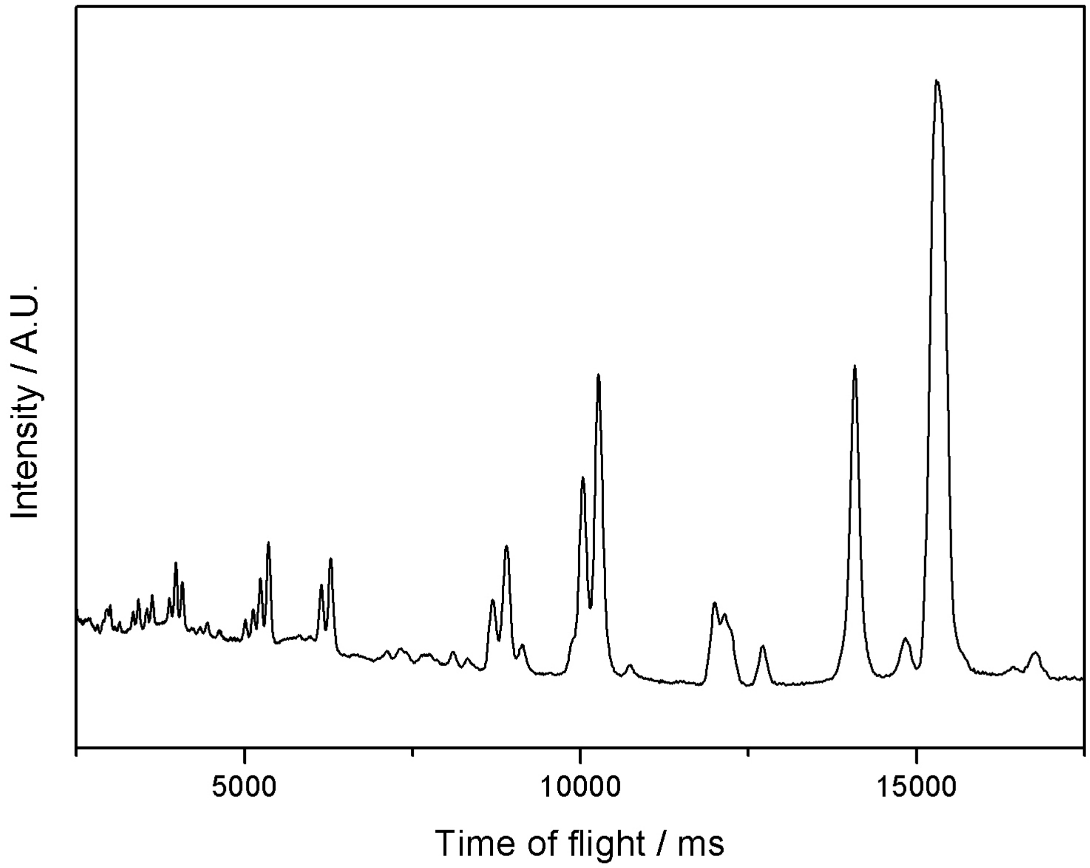

Figure 3.2: An example of the diffraction data for Li(ND$_3$)$_3$BD$_4$, collected using bank 4 of GEM. Showing significant peak overlap and steel reflections that appear as the intense doublets at ca. 10,000 ms and below.

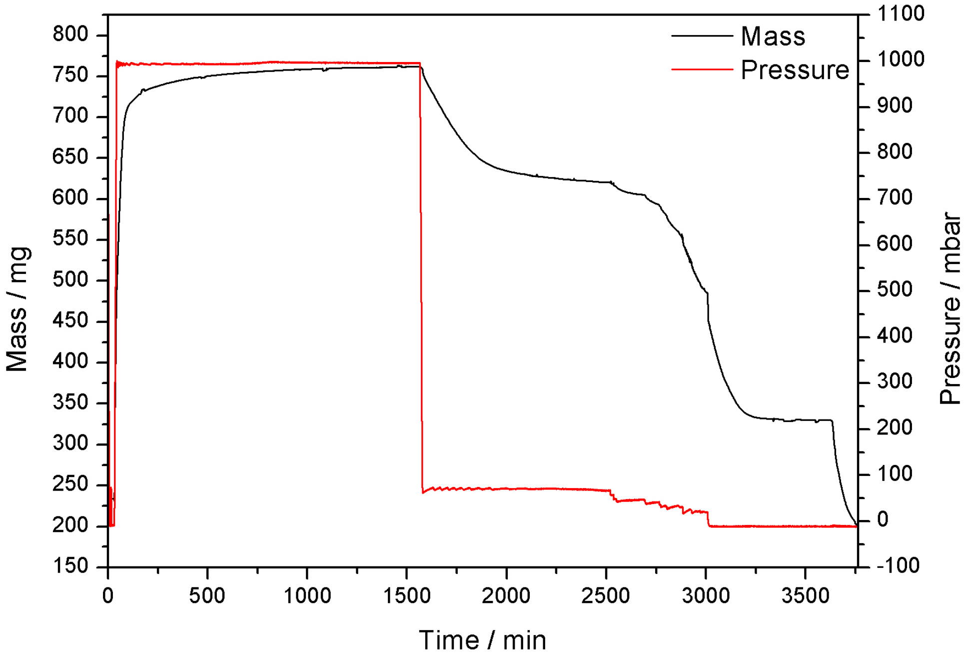

Figure 3.3: The IGA$^{\mathrm{n}}$ data from the HRPD experiment. Showing the sample mass, ammonia pressure and isolation of the phases $\mathrm{Li(ND_3)_nBD_4}$ at various pressures.

3.3 Lithium Borohydride Monoammine

The monoammine of lithium borohydride exists at room temperature, with a minimal or zero overpressure of ammonia — ex-situ samples were produced as described in Section 2.5, by evacuating a sample of $\mathrm{Li(NH_3)}_{n\,\geq\,1}\mathrm{BH_4}$ to 1×10^{-2} mbar — thus it has been relatively simple to use a variety of techniques to investigate its structure. The use of a variety of techniques is necessary in order to confirm assumptions made about the structure and to reduce the uncertainty arising from the sole use of diffraction data to solve structures. The principle assumptions to confirm are the presence of NH_3 and BH_4 (and not reaction products such as NH_2BH_3) and the stoichiometry of the samples.

3.3.1 Nuclear Magnetic Resonance

The ^{1}H NMR spectra of $Li(NH_3)BH_4$ in THF-d_8 is shown in Figure 3.4 and confirms the presence of the NH_3 molecule and BH_4^- anion. The peaks are assigned as follows: δ ^{1}H(300Hz): 0.745 (3H, NH_3); 0.081, 0.351, 0.622, 0.892 (1:1:1:1 quartet, $^1J(^{11}B\,^1H)$ = 81Hz) (BH_4, ^{11}B); 0.214, 0.304, 0.395, 0.485, 0.575, 0.665, 0.756 (1:1:1:1:1:1:1 multiplet, $^1J(^{11}B\,^1H)$ = 27Hz) (BH_4, ^{10}B). The spectra shows a classic splitting of the BH_4 signal, consisting of 4 and 7 peak multiplets in the ratio of 4:1 caused by coupling of ^{1}H to the 80 % naturally abundant ^{10}B (with spin I = 3/2) and 20 % naturally abundant ^{11}B (with spin I = 3). The peak corresponding to the ammonia molecule is broad, and no coupling between ^{1}H and ^{15}N or ^{14}N is observed. Given that THF solvent peaks appear despite using a deuterated solvent, it is possible that proton exchange between the solvent and ammonia has occured resulting in a scrambling of the expected splitting, and peak broadening. The broadening could also be due to the coupling of the protons and the ^{14}N nuclear spin-lattice through interaction of the ^{14}N quadrupolar moment with the axial electric field gradient of the ammonia molecule. The importnat result with respect to the Thesis is that the observation of BH_4 and NH_3 signals in solution suggests that these species exist in the solid state and that no aminolysis or other competing reaction has occurred. The integrated areas below the NH_3 and BH_4 peaks should be in the ratio 3:4, the observed ratio of 2.9:4 may be due to some loss of ammonia on solvation with the possible addition of some proton exchange between the solvent and ammonia molecules.

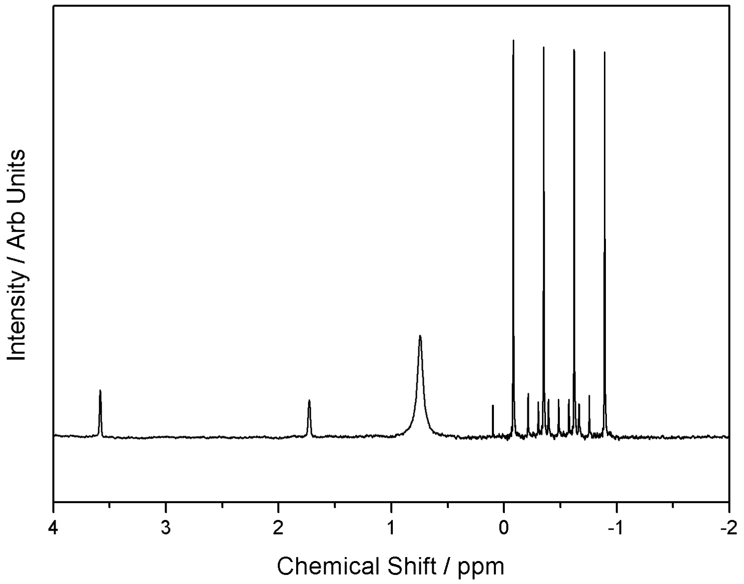

Figure 3.4: The THF-d_8 solution state ^1H NMR spectra of $Li(NH_3)BH_4$, confirming the presence of NH_3 (broad singlet at 0.7 ppm) and BH_4 (1:1:1:1 quartet and multiplet centered around -0.5 ppm), referenced against the THF peaks at 1.73 ppm and 3.58 ppm.

The solid state ^{11}B NMR spectra is shown in Figure 3.5. A single central transition at ca. -41 ppm is observed and confirms the presence of a single boron environment. The value of the chemical shift is is very similar to that found for $LiBH_4$. This infers not only that the BH_4^- anion is present in the solid but also that it is found in a very similar electronic environment to that in $LiBH_4$. The additional minor peaks in the spectra are spinning side bands as described in Section 2.10.

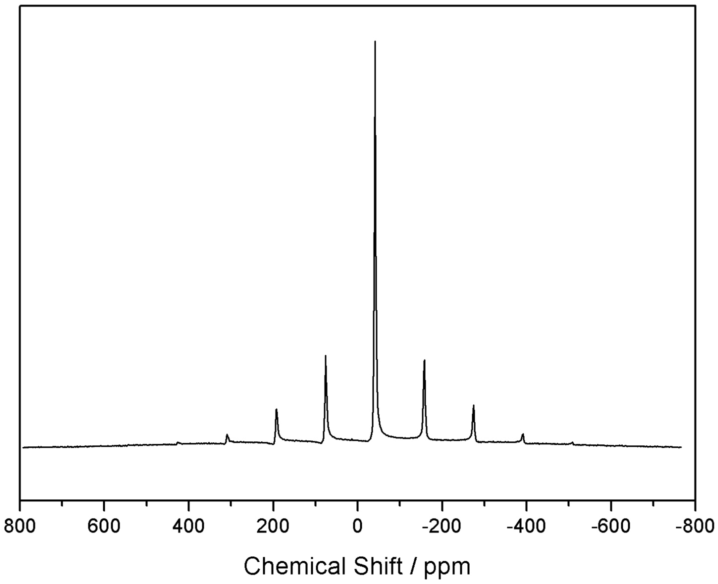

Figure 3.5: The solid state ^{11}B NMR spectra of $Li(NH_3)BH_4$ showing a single central transition at ca. -41 ppm.

3.3.2 Thermogravimetric Analysis

Thermogravimetric analysis data are shown in Figure 3.6. Analysis was carried out using the IGA^n apparatus without neutron diffraction, data were collected in 'outgas' mode using a heating rate of 2 $°Cmin^{-1}$. Mass loss was observed to begin at T_o = 47 °C, with the rate of mass loss beginning to decrease at 140 °C and the final mass loss plateau reached at approximately 180 °C. The mass trace is uneven, which it is thought is due to gas release causing an uneven jumping of the fairly small powder sample. The total mass loss reaches approximately 40 wt% and it is most likely that this corresponds exclusively to the loss of ammonia. The reduction from the theoretical loss of 44 wt% may be due to incomplete initial formation of $Li(NH_3)BH_4$ or its partial decomposition during storage. Complete formation of the amidoborane side product, $LiBH_3NH_2$, upon decomposition would result in a mass loss of only 5 wt% so this is clearly not a major product. However the slightly lower mass loss of than expected could be due to its formation at higher temperatures, in this case 90 % of the ammonia would be given off, with 10 % forming the amidoborane. If this were the case then the ammonia storage potential upon subsequent ammonia cycles may be dramatically reduced. The decomposition product and reversibility are discussed further in Section 3.7.

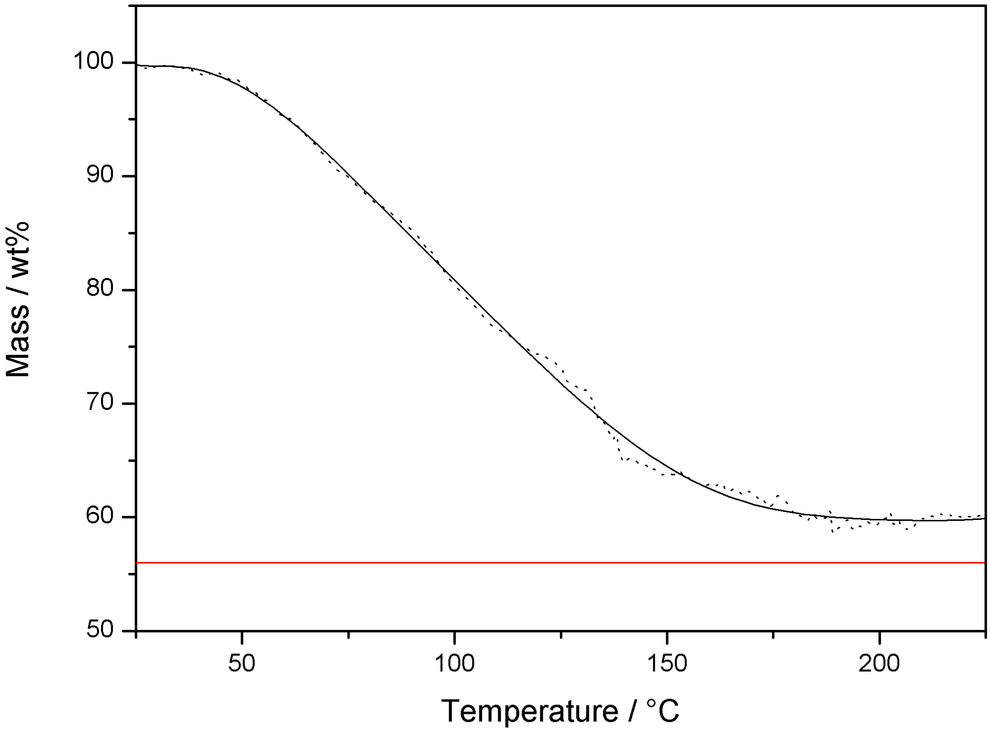

Figure 3.6: IGA data for Li(NH_3)BH_4, showing the sample mass in black and the mass loss corresponding to complete conversion to $LiBH_4$ in red. The raw mass loss data are shown as a dotted line, while fitted data are shown as a solid line.

3.3.3 Diffraction

Although the standard synthetic method produced a polycrystalline sample, it was also possible to grow single-crystals of Li(NH_3)BH_4 using the alternative method described in the Chapter 2. The growth of single-crystals was possible due to the formation of a liquid phase on reduction of ammonia vapour pressure during synthesis. It is expected that this liquid phase is an $LiBH_4 \cdot nNH_3$ solution, and slow evaporation of NH_3 from this solution allows for crystal growth. It is highly possible that with careful selection of evaporation temperatures and pressures, single-crystals of all the phases may also be grown, though this was not attempted. Single-crystals varied in size, with largest observed dimensions of approximately 2 × 1 × 1 mm.

X-ray Powder Diffraction

Bragg peaks in the X-ray powder diffraction pattern were indexed to a new orthorhombic unit cell. A Pawley refinement was performed in DASH using the holosymmetric orthorhombic space group *Pmmm* and resulted in lattice parameters of a_I = 5.96784(3) Å, b_I = 4.46339(2) Å, c_I = 14.34206(8) Å and a cell volume V_I = 382.143(2) Å^3. The extracted integrated intensities were analysed for systematic absences using a Bayesian ranking procedure within DASH. This yielded $Pn-a$ as the most likely extinction symbol, which corresponds to space group $Pn2_1a$ and its centrosymmetric supergroup *Pnma*. In principle, with single crystal diffraction, it is possible to discriminate between these two space groups by an analysis of intensity statistics. However, with powders it is generally not possible to detect the presence or absence of a centre of symmetry. In such cases, it is most reasonable to presume that the material is centrosymmetric unless there is a strong physical reason to assume otherwise or if further refinement results in a significantly superior fit using the non-centrosymmetric space group.

Comparison with the parent $LiBH_4$, which belongs to the space group *Pnma*, with a_0 = 7.17858(4) Å, b_0 = 4.43686(2) Å and c_0 = 6.80321(4) Å, cell volume V_0 = 216.685(3) Å^3, shows a close similarity of the b-axis parameters and suggest a structural relationship between the two phases. Comparison of the unit-cell volumes for $LiBH_4$ and $Li(NH_3)BH_4$ suggests that Z = 4 formula units per unit cell for $Li(NH_3)BH_4$ as is the case for $LiBH_4$. This leaves the approximate excess volume for each NH_3 molecule of (382 − 217)/4 Å^3 = 41 Å^3 which is consistent with the volumes of ammonia molecules seen in other ammines.[33]

While it is attractive to begin to model $Li(NH_3)BH_4$ based upon potential structural similarities with $LiBH_4$, a more general approach is to reduce the symmetry to $Pn2_1a$ and then solve the structure. Unusually, there are no special positions in $Pn2_1a$ implying that global optimisation methods will explore all molecular orientations and positions, and simultaneously explore both $Pn2_1a$ and $Pnma$. The structure was solved using the simulated annealing process within the program DASH, which (as described in Section 2.6.4) uses a Z-matrix formalism to describe molecule conformation in terms of internal coordinates. Three Z-matrices were used that described *i*) one BH_4^- tetrahedral unit; *ii*) one NH_3 molecule; and *iii*) one Li^+ ion. A global minimum was repeatedly found that placed all three non-hydrogen atoms at $(x, \sim 3/4, z)$ close to the mirror plane in $Pnma$ — this is also found in $LiBH_4$. Locating these atoms at $(x, 3/4, z)$ and adopting the space group $Pnma$, the structure was refined using the Rietveld method in TOPAS. No improvement in the Rietveld fit was found by retaining the lower $Pn2_1a$ symmetry. Given the difficulty in obtaining precise hydrogen positions using X-ray powder diffraction, constrained BH_4^- and NH_3 geometries were used during Rietveld refinement. Ideal tetrahedral coordination was enforced for BH_4^-, while all N−H distances and H−N−H angles were restrained to be equivalent to a free NH_3 molecule. The final results of the refinement are given in Appendix E.1, the final fit to the data is shown in Figure 3.7 and the structure is discussed in Section 3.3.5.

X-ray Single Crystal Diffraction

Although the structure has already been solved from the powder data, the superior structural solution possible with single-crystal data serves as a useful check of the structure refined from the powder data. Furthermore the use of single-crystal data allows for far more accurate positioning of the hydrogen atoms and the use of more sophisticated models, with fewer constraints, compared to those which are sensible to use in analysis of powder data. The structure was solved (with the assistance of Dr. Francesca Fabbiani) by direct methods using the program SIR92, and refined against

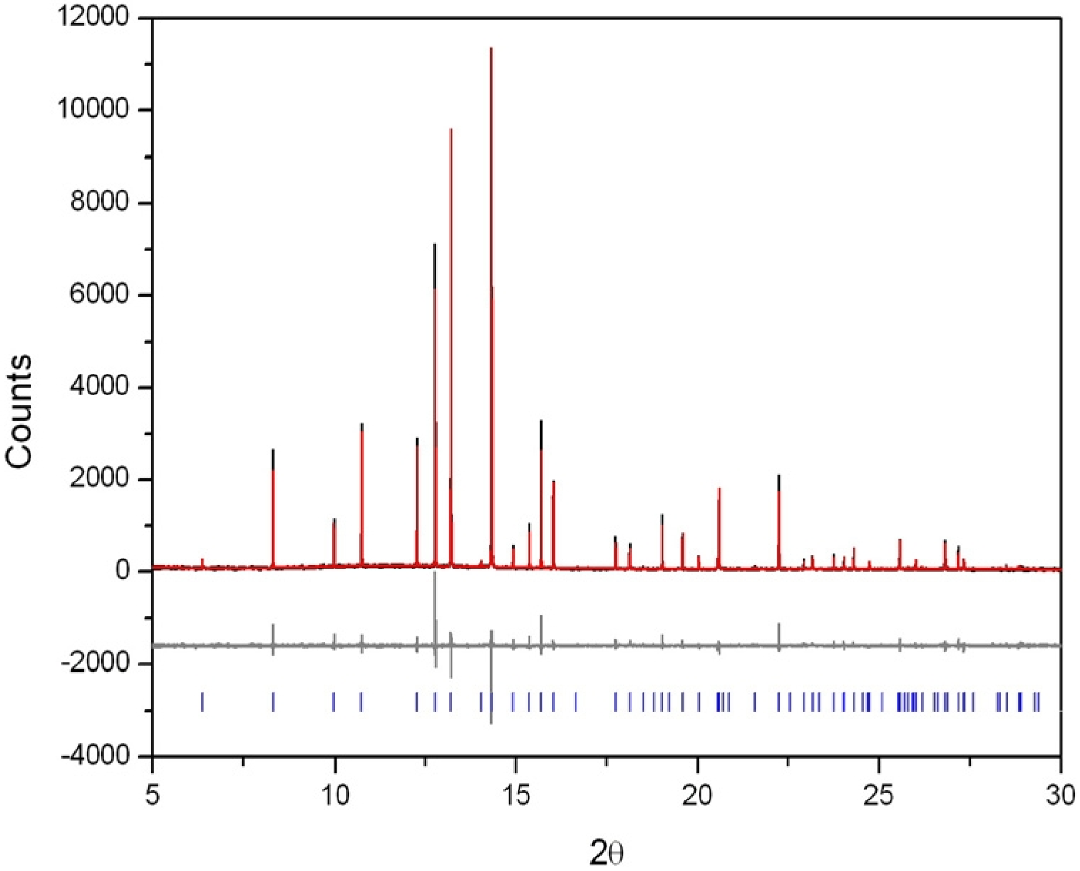

Figure 3.7: Final fit to the data for Rietveld refinement of the $Li(NH_3)BH_4$ model to X-ray powder diffraction data collected at the ESRF with a wavelength $\lambda = 0.79825$ Å. Experimental data are shown in black, calculated in red with the difference in grey, tick marks show the expected positions of Bragg reflections.

F^2 using all the available data with the program CRYSTALS (described in Section 2.6.4). All non-H atoms were modelled with anisotropic displacement parameters. H atoms attached to B were located in difference Fourier maps and their positions and isotropic atomic displacement parameters freely refined. The difference Fourier maps indicated disorder of the ammonia H atoms, thus three refinement models with varying levels of disorder associated with the NH_3 molecule were investigated; *i*) a model with ordered hydrogen atoms; *ii*) a model with disordered hydrogen atoms; and *iii*) a model with the hydrogen atom electron density distributed evenly around a ring.

The σ site symmetry of N is only compatible with the molecular C_{3v} symmetry of the NH_3 molecule given an alignment of one of the N−H bonds (in this case $N1 - H5$) on the $(x, 1/4, z)$ mirror plane. This is the basis for the formation of the ordered model, which features large isotropic temperature factors of the NH_3 hydrogen atoms (see Figure 3.8a). The disordered model allows for positioning of one H atom (H5) with a site occupancy of 0.5 off the $(x, 1/4, z)$ mirror plane thus producing 4 hydrogen sites as shown in Figure 3.8b. Comparison of the two models reveals that the refined isotropic thermal parameter for H5 is smaller in the disordered model (0.041 Å^2, c.f. 0.114 Å^2 in the ordered model), as is the R-factor (3.0 %, c.f. 3.7 % in the ordered model), at the expense of only one extra least-square parameter. Despite this improvement, the resulting model clearly gives unreasonable H−N−H bond angles and the thermal parameter for H4 is still too large. A satisfactory disordered model for the NH_3 molecule could not be obtained with the available data. An alternative description of disorder, which has been successfully implemented in the program CRYSTALS, involves modelling an annulus of continuous electron density as shown in Figure 3.8c. The occupancy of the annulus was set to 3 and the radius of the annulus was refined to 0.825(10) Å, corresponding to an agreeable N−H bond distance. An isotropic temperature factor, i.e. the thickness of the annulus, as well as the declination angle between the ring normal and the z-axis of the orthogonal coordinate system were also successfully refined. A final R-factor of 3.2 % was obtained, which though slightly higher than that for the disordered model allows for a chemically reasonable NH_3 molecule. Overall, the experimental evidence suggests there is a high level of rotational disorder of the NH_3 molecule as observed in other compounds with similar NH_3 coordination.[95] Though it is not possible to tell if this disorder is static or dynamic in its nature. The successful refinement of an annulus of electron density could indicate almost full spinning for $Li(NH_3)BH_4$ at 150 K.

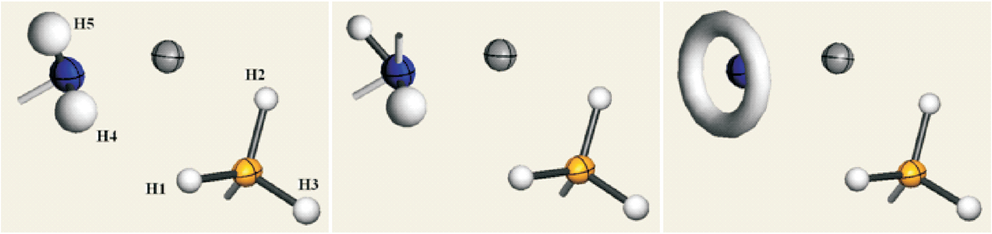

Figure 3.8: Models refined against the X-ray single-crystal diffraction data, from left to right the; a) ordered model; b) disordered model; and c) annulus model.

Full details of the refinement are given in Table 3.2, and the structure is discussed in Section 3.3.5. It is interesting to note at this stage that the presence of local N−H···H−B interactions is uncertain and cannot be unequivocally established given the presence of disorder. The relevant data for both the ordered and disordered models are given in Table 3.1. In both models, N−H···HB and B−H···HN angles fall within the range seen in other compounds exhibiting dihydrogen bonds. However in the ordered model, the minimum NH···HB distance is 2.425 Åwhich, greater than the sum of van der Waals radii for the H atoms, suggests the absence of dihydrogen bonding. On the contrary when the disordered model is analysed, the minimum NH···HB distance is 2.282 Å, which does suggest some degree of dihydrogen bonding and highlights the importance of establishing the nature of the disorder within these systems.

Table 3.1: Observed H···H distances and angles in Li(NH$_3$)BH$_4$, obtained from refinement of the ordered and disordered models against the X-ray single crystal diffraction data.

Distance Description	Distance / Å	Angle Description	Angle / °
	Ordered Model		
$H_4 \cdots H_1$	2.457(19)	$N-H_4 \cdots H_1$	159.7(3)
$H_4 \cdots H_3$	2.54(2)	$N-H_4 \cdots H_3$	143.0(15)
$H_5 \cdots H_3$	2.425(17)	$N-H_5 \cdots H_3$	146.2(8)
Mean	2.486	Mean	150.34
		$B-H_1 \cdots H_4$	102.7(7)
		$B-H_3 \cdots H_4$	98.5(6)
		$B-H_3 \cdots H_5$	156.8(8)
		Mean	104.4
	Disordered Model		
$H_4 \cdots H_1$	2.448	$N-H_4 \cdots H_1$	163.0
$H_4 \cdots H_3$	2.567	$N-H_4 \cdots H_3$	142.1
$H_5 \cdots H_3$	2.282	$N-H_5 \cdots H_3$	166.1
Mean	2.432	Mean	157.1
		$B-H_1 \cdots H_4$	104.1
		$B-H_3 \cdots H_4$	98.7
		$B-H_3 \cdots H_5$	146.4
		Mean	116.4

Table 3.2: The atomic coordinates obtained from the Rietveld refinement of the ordered model of Li(NH$_3$)BH$_4$ against X-ray single-crystal diffraction data.

atom	site	x	y	z	B_{iso} / Å^2
N	N1	0.6081(4)	0.7500	0.6514(1)	5.9(1)
B	B1	0.9059(4)	0.7500	0.3993(1)	4.6(1)
Li	Li1	0.8903(8)	0.7500	0.5752(3)	4.7(2)
H	H1	0.754(2)	0.7500	0.451(1)	5.5(3)
H	H2	0.073(2)	0.7500	0.442(1)	5,5(3)
H	H3	0.898(1)	0.536(2)	0.352(1)	5.5(3)
H	H4	0.519(2)	0.584(1)	0.632(2)	5.5(3)
H	H5	0.585(3)	0.7500	0.717(1)	5.5(3)

3.3.4 Geometry-optimised Structure

The single-crystal structure from the ordered model was used as a starting point for DFT geometry optimisation calculations. These calculations were performed due to the requirement for minimal atomic forces to be present in the structure used for phonon calculations, which in-turn were necessary to perform the vibrational spectroscopy analysis discussed in Section 3.3.6. Recently Zhong et. al.,[96] reported a close agreement between their optimised atomic positions and the atomic positions refined from the X-ray powder diffraction data discussed in Section 3.3.3. The optimised atomic positions reported here are also close to the those experimentally observed and are given in Table 3.3. The calculations were performed with no symmetry constraints, but (within a tolerance of 0.001 Å) no change from the *Pnma* starting symmetry was observed. The similarities between the two structures are highlighted by the small change in bond lengths upon optimisation: B−H changes from 1.151 Å to 1.227 Å, N−H changes from 0.845 Å to 1.032 Å , Li−N changes from 2.014 Å to 2.041 Å , and Li−B changes from 2.550 Å to 2.522 Å . The observed global increase in bond lengths at the zero-point energy suggests disorder within the system and significant atomic motion resulting in the geometric mean of the atomic positions being observed in the diffraction data, as discussed in Section 2.12. Significantly the N−H bond length shows the largest change suggesting a large amount of rotational disorder associated with the NH_3 molecule.

3.3.5 Structural Description and Discussion

As mentioned in Section 3.3.3, the structure of $Li(NH_3)BH_4$ shows many similarities with that of $LiBH_4$. These similarities are particularly clear when both structures are viewed perpendicular to the common short b-axis, as shown in Figure 3.9. The lithium cations in $LiBH_4$ are tetrahedrally coordinated by four BH_4^- anions while each BH_4^- anion is coordinated by four Li^+ cations. In $Li(NH_3)BH_4$, each Li^+ cation

Table 3.3: The atomic coordinates from the DFT optimised $Li(NH_3)BH_4$ structure.

atom	site	x	y	z
N	N1	0.57232	0.75000	0.64392
B	B1	0.92538	0.75000	0.40042
Li	Li1	0.87440	0.75000	0.57321
H	H1	0.74378	0.75000	0.44339
H	H2	0.93526	0.52798	0.34988
H	H3	0.08657	0.75000	0.45594
H	H4	0.47030	0.56647	0.63030
H	H5	0.59931	0.75000	0.71559

is tetrahedrally coordinated by three BH_4^- anions and one NH_3 molecule while each BH_4^- anion is linked to three Li^+ cations and four NH_3 molecules. The BH_4^- anion exhibits η^2 bonding to Li^+, with Li−B bond distances of 2.474 Å and 2.545 Å. The observed BH···HN bond distances are 2.160 Å and 2.284 Å, these suggest the presence of some dihydrogen bonding though non that is a great deal stronger than Van der Waals forces. These distances are taken from the optimised structure as it provides the most realistic bond lengths when considering a potentially disordered system. In $LiBH_4$, the $Li(BH_4)_4$ tetrahedra are linked in edge-sharing chains that run along the b-axis and are vertex-linked to neighbouring chains. $Li(NH_3)BH_4$ is composed of similar chains of edge sharing $Li(NH_3)(BH_4)_4$, tetrahedra though the polarity of the NH_3 molecule stops vertex-linking between chains resulting in the increased separation seen in Figure 3.9. The structures in Figure 3.9 show polyhedra of nearest neighbours to the Li^+ cation, more standard molecular views are presented in Figures 3.30 and 3.30, the immediate tetrahedral coordination of the Li^+ cation is shown clearly in Figure 3.14.

3.3.6 Inelastic Neutron Scattering and Raman Spectroscopy

Vibrational spectroscopy data (INS and Raman spectroscopy) were collected as described in Chapter 2 Sections 2.8 and 2.9. The calculated and experimental INS

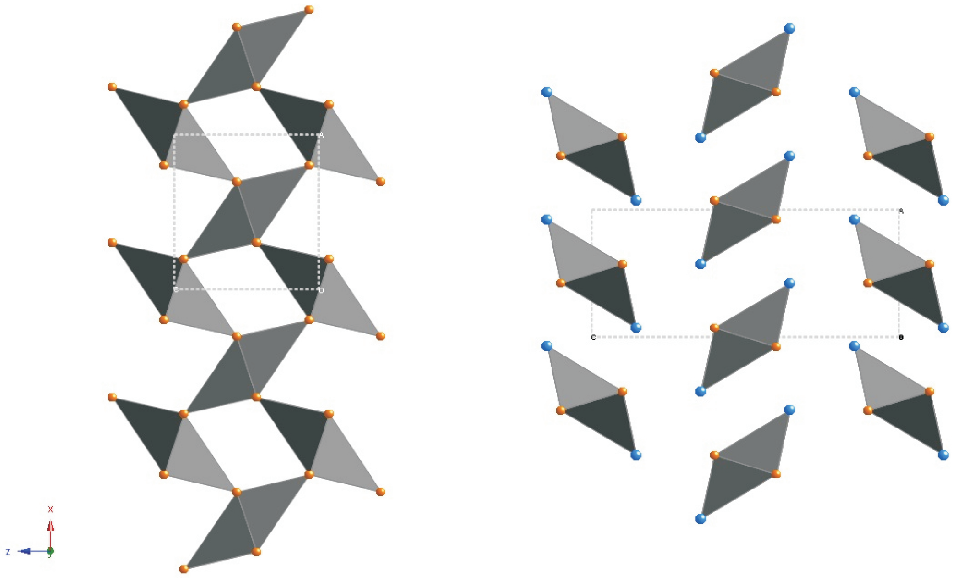

Figure 3.9: A comparison of the $LiBH_4$ and $Li(NH_3)BH_4$ structures, viewed slightly off the y-axis. Hydrogen atoms are omitted for clarity, Li atoms are shown in grey, boron in brown and nitrogen in blue. $Li(NH_3)(BH_4)_3$ polyhedra are shown in grey.

spectra for $Li(NH_3)BH_4$ are shown in Figures 3.10 and 3.11, with the equivalent Raman spectra shown in Figure 3.13. There is a good qualitative agreement between the calculated and observed spectra, though some discrepancy between the absolute (observed and calculated) frequencies. These differences are expected to some degree given that the calculated spectra are based on phonon modes calculated at 0 K, while the experimental spectra were collected at 20 K and 298 K for the INS and Raman data respectively. The calculation of these modes is non-trivial and errors of the magnitude seen in this work are common in many other reported studies.[97,98] A potential source of error in comparison of the calculated and observed INS spectra is caused by the use of naturally abundant B samples rather than the isotopically enriched, and preferable, ^{11}B for which the spectra simulation methods at ISIS are based. Modes involving B atoms will lack intensity in the observed spectra due to ^{10}B neutron absorption, and in addition the lower mass of ^{10}B will lower the frequency of certain modes. The presence of lower frequency modes of ^{10}B will have a line broadening effect due to superposition of two very similar spectra, though to some extent this will be negated by the minimal intensity of ^{10}B modes caused by absorption. However, the dominant features of spectra will be caused by the 80 % abundant ^{11}B and more importantly the hydrogen atoms connected to the boron (involved in all the boron modes), thus both the observed and calculated spectra should be similar. The combination of Raman and INS spectra show the vibrational behaviour of the compound in detail across a large range of frequencies, to a degree that would be hard to achieve using one technique alone. An important conclusion drawn from the strong agreement between the observed and calculated frequencies in both spectra is that the calculated phonon modes are realistic. A complete table of these calculated modes and their assignments is provided in Appendix D.1.

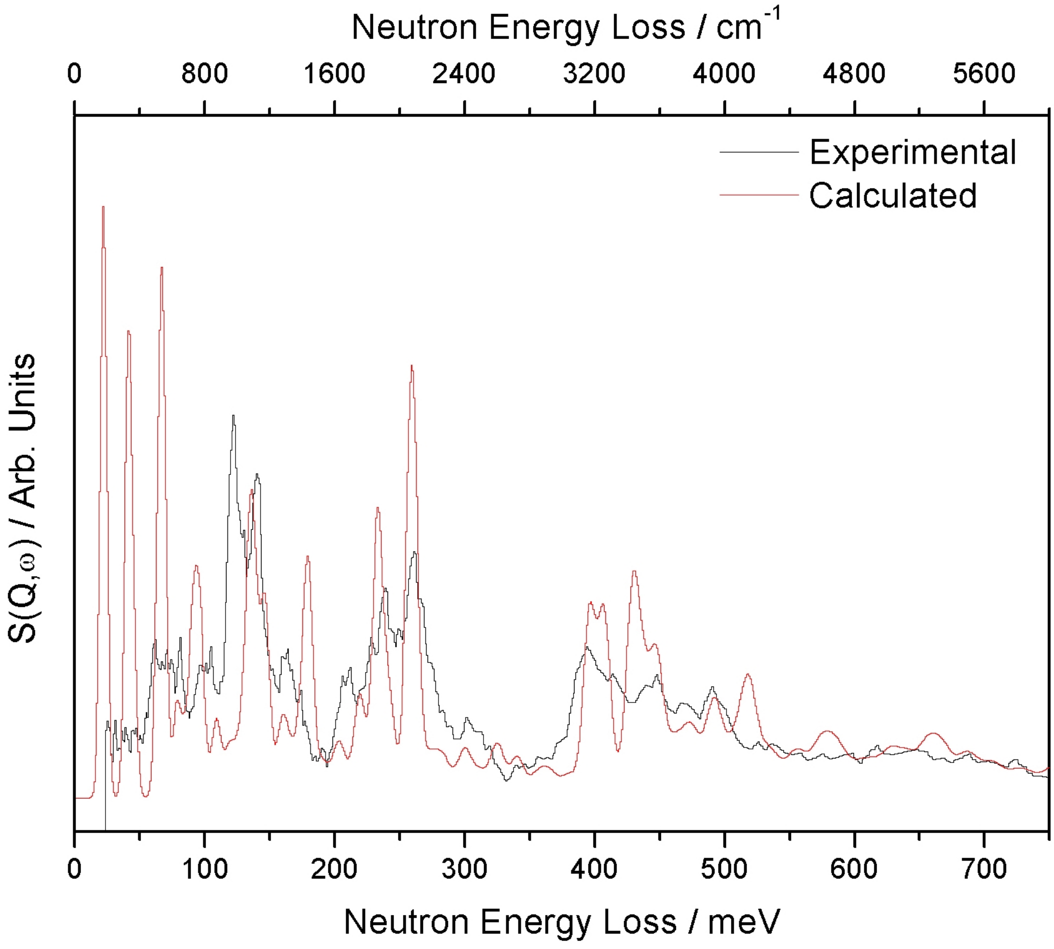

Figure 3.10: The experimental (black) and calculated (red) INS spectra for $Li(NH_3)BH_4$, shown between 0 meV and 750 meV.

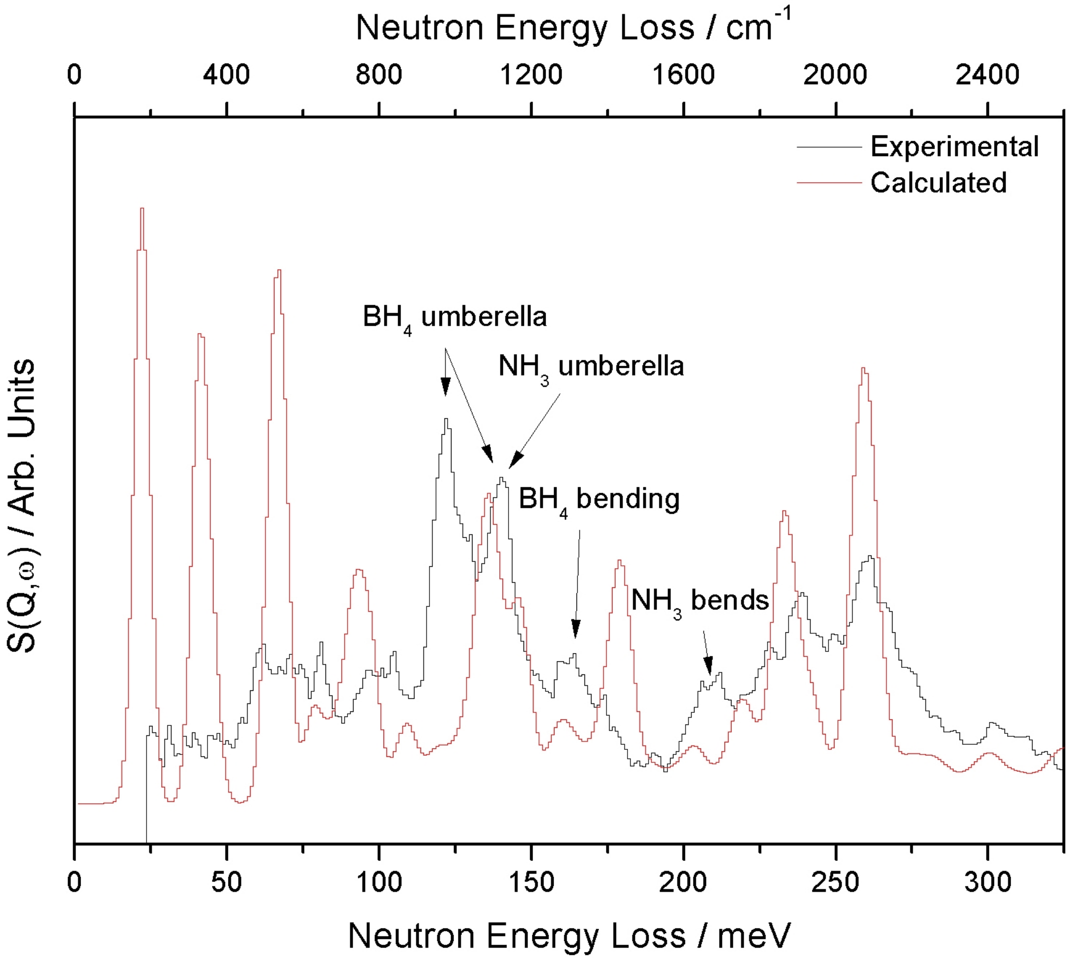

Figure 3.11: The experimental (black) and calculated (red) INS spectra for $Li(NH_3)BH_4$, shown between 0 meV and 350 meV with the position of important modes labelled.

One of the most interesting features of the calculated modes are those at low and negative frequencies. Negative modes were calculated at -44 cm^{-1} and -21 cm^{-1}, and while these are often indicative of an inherent instability in the calculated structure in this case they are more suggestive of the atomic motion present under normal conditions. The mode at -21 cm^{-1} corresponds to the in-phase libration of ammonia molecules as shown in Figure 3.12, whilst the mode at -44 cm^{-1} shows less well defined anti-phase libration. The implication of this and the observation of a number of other low frequency librational modes at 24 cm^{-1}, 42 cm^{-1} and 68 cm^{-1} is that there is a non or minimal barrier to the rotation of the ammonia molecule. This corroborates the disorder seen in the single-crystal diffraction analysis.

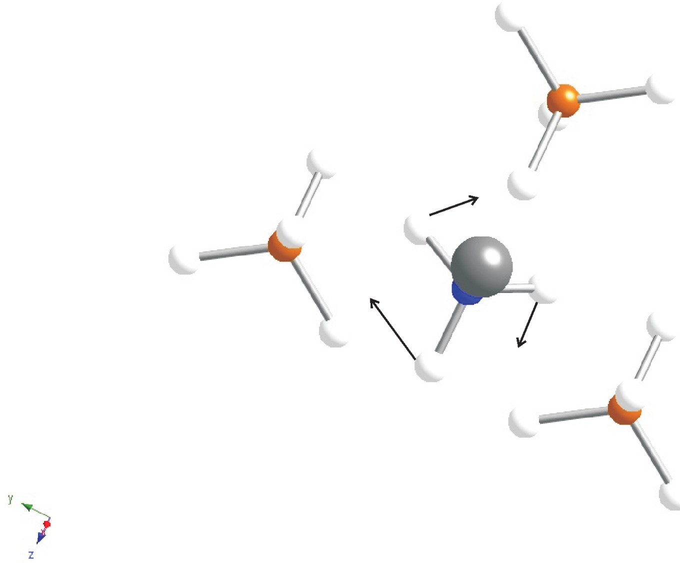

Figure 3.12: A depiction of the calculated mode at -21 cm^{-1} in Li(NH$_3$)BH$_4$, with arrows representing the eigenvectors of the mode. Lithium is shown in grey, boron in brown, nitrogen in blue and hydrogen in off-white.

A notable feature of the Raman spectra is the mode observed at around 3215 cm^{-1}, which does not appear in the calculated spectra. The spacing between the principle mode at 3296 cm^{-1} and the side-band is around 81 cm^{-1}. It is suggested that this side-band is caused by vibration-rotation coupling between NH$_3$ stretches and rotations. Inspection of the INS data suggests that the excited mode

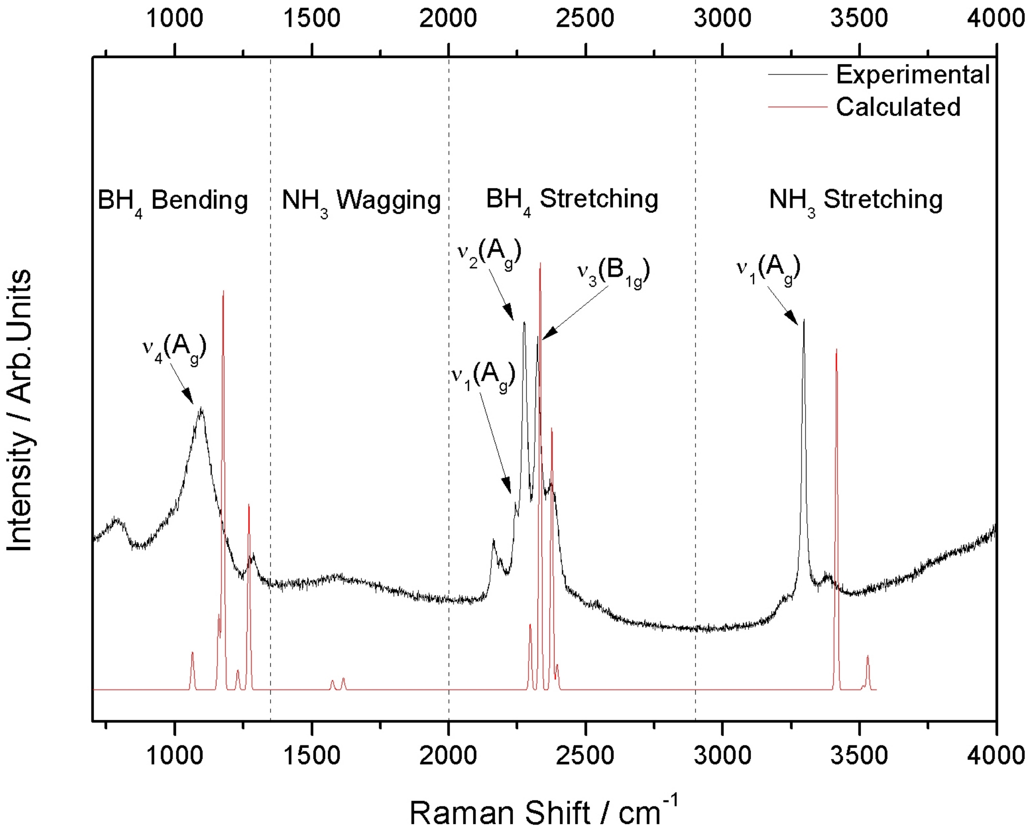

Figure 3.13: The observed and calculated Raman spectra for $Li(NH_3)BH_4$ with the position of important modes labelled.

is the one that appears at 81 cm^{-1}, there are several calculated NH_3 librational modes in this region appearing at 68 cm^{-1}, 94 cm^{-1} and 98 cm^{-1}.

In Section 2.12, the process of calculating the Gaussian probability distribution from phonon modes is described; Figure 3.14 shows the result of these calculations at 150 K and 298 K in a single $Li(NH_3)(BH_4)_3$ unit. The massive thermal ellipsoids of the NH_3 hydrogen atoms compared to the B, Li, and N atoms show clearly the low energy barrier to NH_3 rotation and corroborate with the large amount of disorder seen in the diffraction data at 150 K. The image of the 298 K structure suggests that almost unhindered spinning of the ammonia molecule occurs at room temperature. This is the case because in practice these ellipsoids would never be a perfect circle and they should never overlap, so in this example they represent a spinning molecule. There is very little change in the size of the thermal ellipsoids on the borohydric hydrogen atoms from 150 K to 298 K, especially in comparison to those of the ammonia molecule. This is to be expected given that it is primarily the low energy and highly populated modes that will contribute to the atomic motions at these temperatures, and not the higher energy BH_4 bends and stretches.

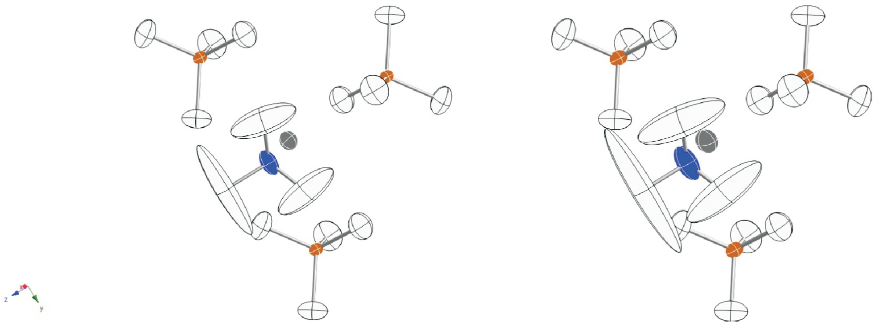

Figure 3.14: The calculated 50 % probability ditributions for the mean squared displacement of atoms at 150 K (left) and 298 K (right) for a single $Li(NH_3)(BH_4)_3$ unit in $Li(NH_3)BH_4$.

In their recent publication, Zhong et. al. suggested that $Li(NH_3)BH_4$ would decompose to give ammonia at 291 K and hydrogen at 371 K.[96] Observation of the mean squared displacements at these temperatures does not offer any real insight into this reaction, as they show no unexpected changes other than a straightforward extrapolation from Figure 3.14. However, a comparison of the BH_4 stretches with those reported by Racu et. al. for $LiBH_4$,[97] confirms a weakening of the B−H bonds that must be caused by the presence of NH_3. The calculated and experimental Raman spectra for $Li(NH_3)BH_4$ at 298 K are shown in Figure 3.13, and a comparison of the observed data and those given by Racu is shown in Table 3.4. While comparison of many of the modes is complex due to the simultaneous movement of NH_3 and BH_4, the internal stretching modes of BH_4 do not involve the motion of any other atoms so may be compared like for like. Given the low resolution of these observed Raman data, and the 2nd overtones of the BH_4 bending modes present in the BH_4 stretching region, unambiguous assignment of the stretching modes via the Raman spectra alone is not possible. However, strong corroboration with the calculated spectra means the strongest modes may be reliably assigned. The $v_1(A_g)$ stretching mode which corresponds to all the H atoms moving in-phase in the B−H direction, features in the Raman spectra for both compounds and is shifted from 2273 cm^{-1} (2392 cm^{-1} calculated) to 2243 cm^{-1} (2298 cm^{-1} calculated) on addition of ammonia to $LiBH_4$. The other directly comparable stretches are also shifted to lower wavenumbers, and provide direct evidence for weakening of the B−H bonds. This weakening is presumably caused by dihydrogen bonding and although a mode that may indicate this through simultaneous B−H and N−H stretching is not seen, a number of modes involving BH_4 and NH_3 libration, rocking, and bending are seen and detailed in Appendix D.1.

The symmetrical $v_1(A_g)$ NH_3 stretching mode, is observed at 3296 cm^{-1} and calculated to appear at 3416 cm^{-1}. There are no convenient comparisons to be made with other ammines in the literature as there was for the BH_4 modes with $LiBH_4$. However, Raman and infra-red spectra of other ammines with comparable coordination environments have been reported. The comparison here is drawn between the symmetrical NH_3 stretch in solid-state compounds where the ammonia molecule is coordinated to the metal centre, the stretch is seen at; 3247 cm^{-1} in $Zn(NH_3)Br_2$, 3260 cm^{-1} in $Ni(NH_3)_6Cl_2$, and 3220 cm^{-1} in $Cd(NH_3)_6Cl_2$.[99–101] These modes are observed at similar wavenumbers to the title compound, but all are at lower wavenumbers, it is suggested that in these compounds, the N−H bond is weakened by M−N interactions that are stronger than the Li−N interactions. This gives some explanation to the hydrogen release observed by Guo et. al., from $M^{II/III}X_{2/3}$ doped $Li(NH_3)BH_4$ which may be a result of $M^{II/III}(NH_3)_n$ complex formation resulting in a weakening of the N−H bond. This combined with the weakening of the B−H bond observed here may lead to low temperature hydrogen release.[102] The reason for the differences seen in the frequencies of these modes would be interesting to investigate further, but is beyond the scope of this Thesis.

Table 3.4: A comparison of the assignment of calculated and observed, internal and external, BH_4 modes in the Raman spectra of $LiBH_4$ (reported by Racu et. al.) and $Li(NH_3)BH_4$ (from this Thesis).[97]

Mode	$Li(NH_3)BH_4$		$LiBH_4$	
	Observed Frequency 298 K / cm^{-1}	Calculated Frequency / cm^{-1}	Observed Frequency 300 K / cm^{-1}	Calculated Frequency / cm^{-1}
		internal bending		
A_g		1063	1090	1063
A_g		1161	1240	1235
$v_4(A_g)$	1270	1286	1320	1312
		internal stretching		
$v_1(A_g$	2243	2298	2273	2329
$v_2(A_g)$	2275	2333	2298	2372
$v_3(B_{1g})$	2324	2377	-	2388
A_g	-	2396	2319	2414

3.3.7 Variable Temperature Powder X-ray Diffraction

In-situ X-ray powder diffraction is an excellent technique for the investigation of the thermal stability of materials. In addition to determining the crystal structure of $Li(NH_3)BH_4$ at room temperature, diffraction data were also collected at the ESRF in 2 °C intervals from 20 °C until the capillary broke at ca. 54 °C. A full Rietveld analysis of $Li(NH_3)BH_4$ was performed at each temperature step and shows a positive thermal lattice expansion seen in Figure 3.15. The expansivities for the a-axis and c-axis are $\Delta a/a = 3.6(1) \times 10^{-4}$ K^{-1} and $\Delta c/c = 5.1(1) \times 10^{-4}$ K^{-1} respectively. Both are essentially linear from 20 °C to 54 °C although there is a small increase in $\Delta c/c$ as the decomposition temperature is approached. The short b-axis has a much smaller expansion as a function of temperature with $\Delta\ b/b = 8(1) \times 10^{-5}$ K^{-1} below 38 °C; above 38 °C, there is a discernible decrease in the rate of expansion which correlates closely with the onset of the decomposition of $Li(NH_3)BH_4$ seen in the TGA (see Section 3.3.2). The c-axis shows the greatest rate of change, this is likely due to the fact that as ammonia leaves the structure voids are opened up. Inspection of the structure shows that it is most compressible along the longest side of the unit cell which thus shows the greatest rate of change.

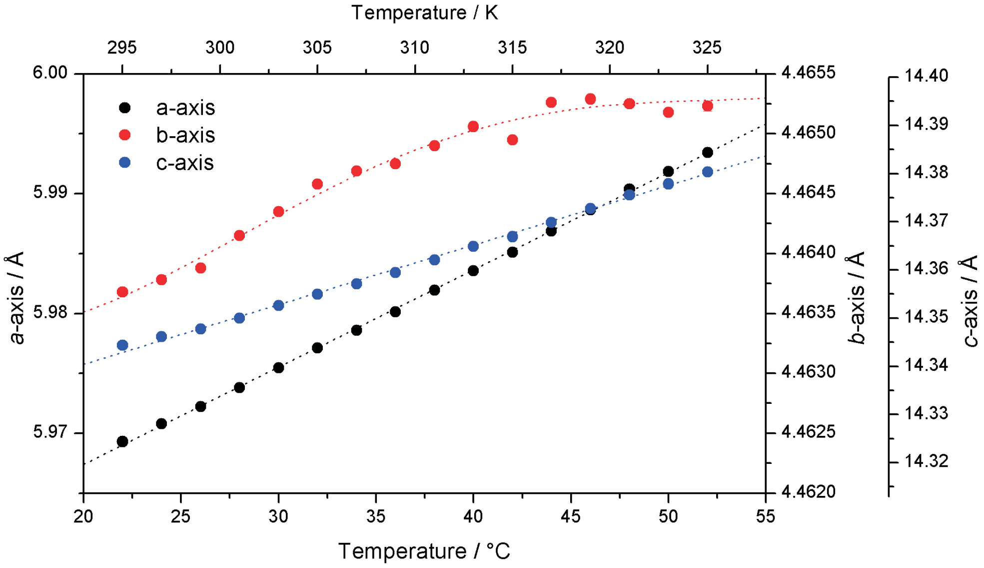

Figure 3.15: The refined lattice parameters for $Li(NH_3)BH_4$ between 38 °C and 50 °C.

The amount of $Li(NH_3)BH_4$ present in the capillary can be assessed by plotting the scale factor associated with this phase as a function of temperature as shown in Figure 3.16. There is a small decrease in the scale factor up to 38 °C and an approximately 30 % decrease between 38 °C and 50 °C. At 50 °C, there is an abrupt drop while at 54 °C there are no detectable Bragg peaks. Examination of the sealed capillary following heating showed that it had exploded, and this explosion is attributed to a release of the absorbed ammonia. This decomposition temperature similar but slightly higher than that observed in the thermogravimetric analysis discussed in Section 3.3.2. Some difference is expected given the difference in experimental conditions, with TGA being carried out under a minimal vapour pressure of ammonia and higher pressure conditions existing inside the sealed capillary. In this case the differences are not worth investigating further, particularly as the thermodynamic conditions inside the capillary are poorly defined and pressure increase within the capillary may, as observed, suppress the decomposition temperature. Also the sample may be at a higher temperature than expected as significant beam heating can occur using high energy synchrotron light sources.

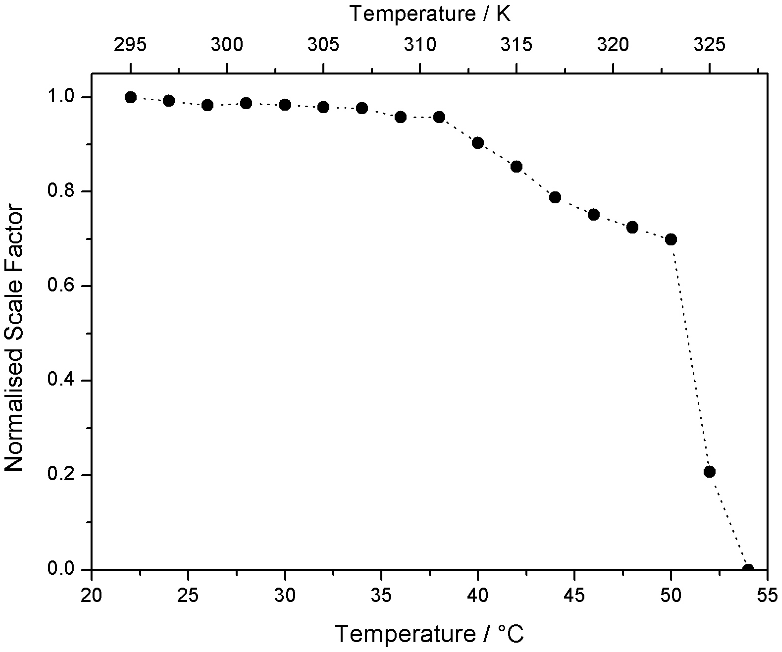

Figure 3.16: The refined scale factors for $Li(NH_3)BH_4$ between 38 °C and 50 °C.

3.3.8 Molecular Dynamics

Molecular dynamics calculations give a unique view of the likely atomic motions at a given temperature. In this case they were used to inspect the molecular motion at 150 K, the same temperature that the single crystal diffraction data were collected. Calculations were carried out as described in Section 2.12 using time steps of 0.5 fs over a total period of 5 ps and with an equilibration period of 3.0 ps. One of the most useful ways to use the results of this calculation is a qualitative analysis based on the animation of molecular motion, analysis of this sort shows that 1) the NH_3 molecule rotates quickly, jumping between low energy sites where it spends most time, in jumps lasting between 0.5 fs and 2 fs; 2) Li^+ cations are the most mobile non-hydrogen atom, moving significantly in the y-direction; and 3) BH_4^- anions do not rotate but oscillate about a fixed position (ie. they are not disordered). Results that can be easily pictures are displayed in Figure 3.17, here it can be seen that there is negligible movement of atoms in the z-direction. However all atoms are highly mobile in the y-direction. An interesting feature of this mobility is that the rows of $Li(NH_3)(BH_4)_3$ tetrahedra diffuse in opposite directions. The movement of the atoms is not obviously correlated, though this could be revealed with further calculation. These results corroborate with all the others discussed in this Section. Though many data may be extracted from these calculations (particularly with respect to ionic mobility and conductivity), such in-depth computational analysis would not befit the main body of this work.

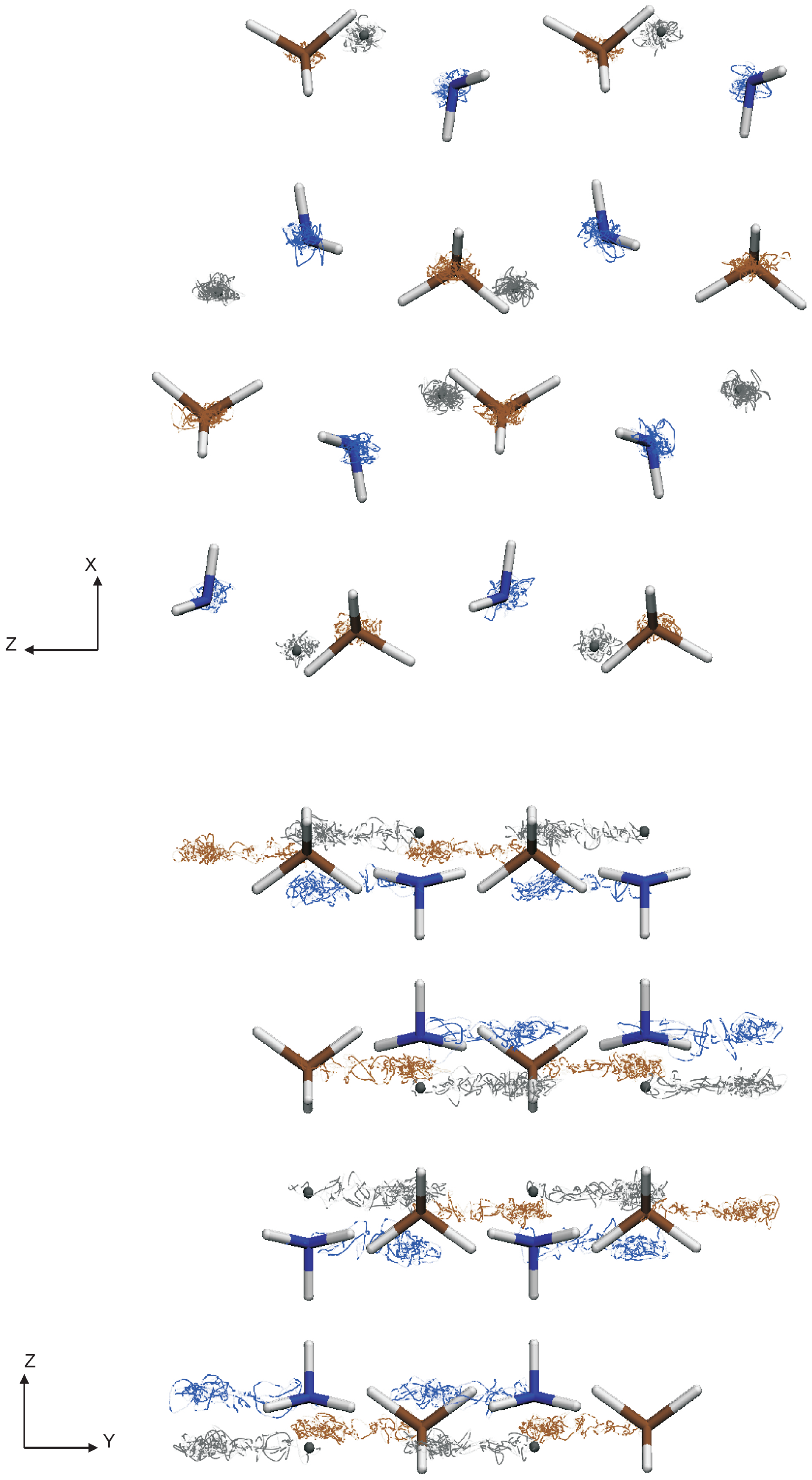

Figure 3.17: The calculated movement of Li (grey), N (blue) and B (brown) atoms in Li(NH_3)BH_4 at 150 K, with points representing atomic positions at 0.5 fs intervals over a period of 5 ps, viewed down the y-axis and x-axis, top and bottom respectively.

3.4 Lithium Borohydride Diammine

Structural studies of lithium borohydride diammine proved challenging; as discussed in Section 1.6 and shown in Figure 3.18, this compound exists as a liquid at temperatures of around 15 °C and above. The IGA$^{\mathrm{n}}$ equipment offers poor control of temperature in this region, and it was not possible to develop appropriate equipment to control ammonia gas pressure at low temperatures. Although a crystalline phase of appropriate mass was briefly observed in the GEM-IGA$^{\mathrm{n}}$ experiment, the quality of the GEM data are not good enough to refine a structural model. By evacuating a sample of $\mathrm{Li(NH_3)_nBH_4}$, where $n \geq 2$, at a temperature of 0 °C it was possible to isolate the $\mathrm{Li(NH_3)_2BH_4}$ phase, however attempts to collect diffraction data at Diamond beamline I11 were unsuccessful due to practical difficulties of loading a sample with such a low melting point into a 0.7 mm capillary tube. Despite these problems the phase was observed in some X-ray powder diffraction data, and was characterised using these data and DFT calculations.

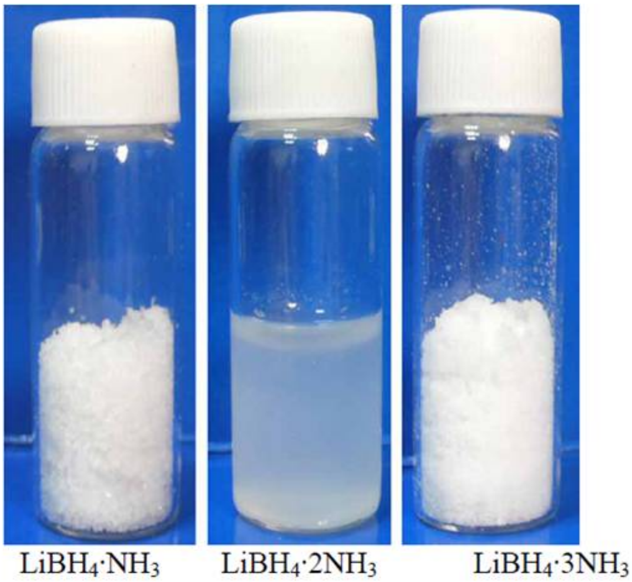

Figure 3.18: The n = 1, 2 and 3 phases of $\mathrm{Li(NH_3)_nBH_4}$ isolated under ammonia pressures by Guo et. al.[102]

3.4.1 Diffraction

X-ray Powder Diffraction

An unknown phase was observed in diffraction data of a sample produced by reaction between liquid ammonia and lithium borohydride at -78 °C. On repeated attempts using the same method only the single phase $Li(NH_3)BH_4$ was observed. The unknown phase was indexed in an orthorhombic cell with refined lattice parameters of a = 9.6227(4) Å, b = 4.44268(2) Å, c = 13.75357(6) Å, and cell volume V = 587.959(4) $Å^3$. Via Pawley refinements and extinction symbol analysis in DASH the space group *Pnma* was chosen. The structure was then solved by simulated annealing in DASH, using four Z-matrices representing one BH_4^- tetrahedral unit, two NH_3 molecules and one Li^+ ion. As was the case with $Li(NH_3)BH_4$, discussed in Section 3.3.3, simulated annealing was performed in the lower symmetry space group $Pn2_1a$ in order to explore a wider number of possible solutions. The obtained solution was then refined using the Rietveld method in TOPAS, and using the centrosymmetric space group, *Pnma*. The similarities with $Li(NH_3)BH_4$ and $LiBH_4$ are seen not only in the unit cells that feature a common short b-axis, but also in the highly similar arrangement of atoms that is also implied in this case by the common space group. The final fit to the data is shown in Figure 3.19, the goodness of fit parameters, $R_{wp} = 12.146$, $R_{exp} = 5.649$, $GOF(\chi) = 2.150$, show a relatively poor fit of the model to the data though observing the fit, this can be largely attributed to the poor fit of the peak at $2\theta = 6.7$ ° despite the good fit to the large number of remaining peaks which give the model increased credibility. It is also strange that this phase is seen to coexist with $LiBH_4$ as one may expect only $Li(NH_3)BH_4$ and $LiBH_4$ to exist together, however the thermodynamics of the phase transitions are not well known and it may be possible for these phases to coexist (especially in a capillary environment). For example, $Li(NH_3)BH_4$ could 'disssociate' into $Li(NH_3)_2BH_4$ and $LiBH_4$ under certain conditions. The similarities to

$Li(NH_3)BH_4$ which along with the similar bond lengths and atomic positions found in the geometry optimisation calculations strengthen the case that this is the correct structure, as discussed further in Section 3.4.3. The structure is discussed furhter in Section 3.4.2.

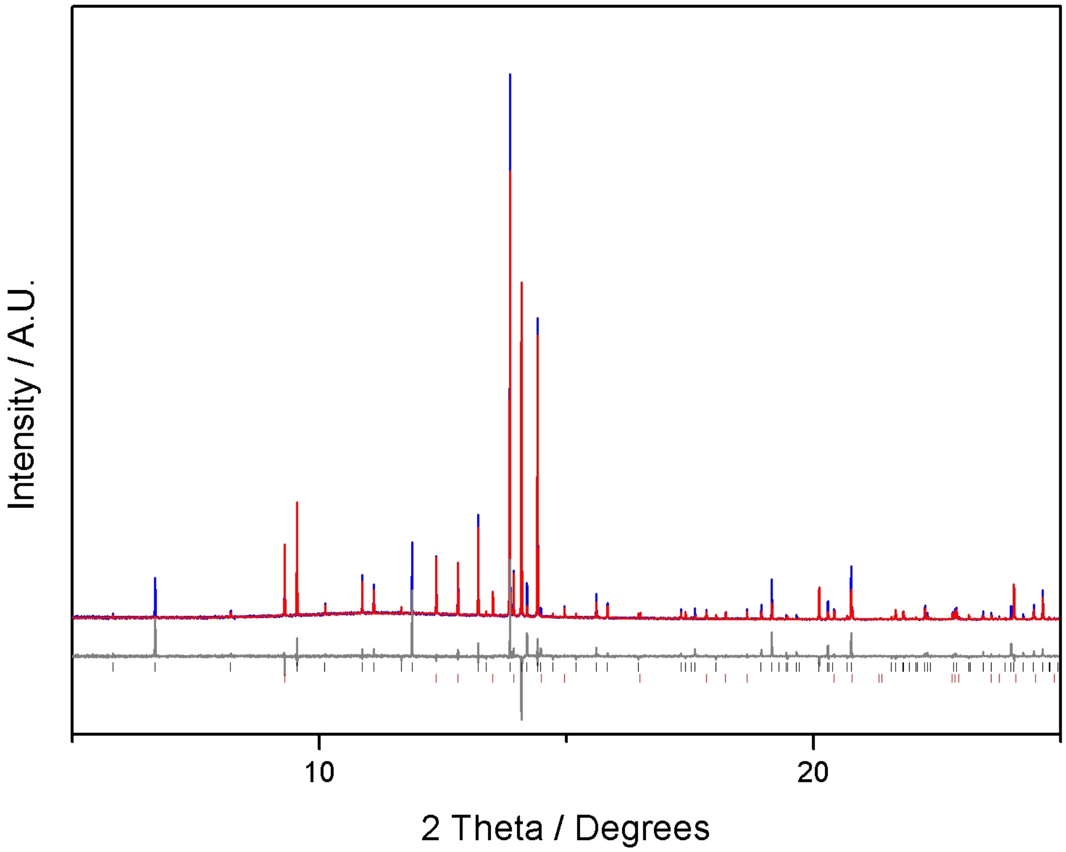

Figure 3.19: Final fit to the data for Rietveld refinement of the $Li(NH_3)_2BH_4$ model to X-ray powder diffraction data, data were collected at the ESRF with a wavelength $\lambda = 0.8022$ Å. Experimental data are shown in blue, calculated in red with the difference in grey, tick marks show the expected positions of Bragg reflections for $Li(NH_3)_2BH_4$ in black and $LiBH_4$ in red.

Neutron Powder Diffraction

A phase was observed in the IGA^n experiment on GEM that corresponds in mass to $Li(NH_3)_2BH_4$, however this phase turned into a liquid so only very limited diffraction data were collected. The phase was observed again in a vanadium can though the conditions of its production are unrepeatable due to an experimental error: the experiment was stopped when $Li^{11}BD_4$ was formed, with the intention of removing the sample from the IGA^n and collecting diffraction data with the sample in a vanadium can. However $Li^{11}BD_4$ was not observed, and it is thought that some residual ammonia in the IGA^n pipework reached the sample causing conversion into the n = 2 phase. The data are also unrefineable due to the small size of the sample recovered from the IGA^n producing a poor signal to noise ratio in the data. Though in both cases it was possible to fit the orthorhombic unit cell described in Section 3.4.1 to the data using a Pawley refinement.

3.4.2 Structure Description

Figure 3.20 shows the structure of $Li(NH_3)_2BH_4$, when this is compared to Figure 3.9 the many similarities with $LiBH_4$ and $Li(NH_3)BH_4$ are clear. Molecular images of the structure are shown in Figures 3.21, 3.31 and 3.35. The diammine consists of chains of edge-sharing $Li(NH_3)(BH_4)_3$ tetrahedra that run along the b-axis, in a near identical fashion to those seen in the monoammine. The additional second ammonia molecule (N2) sits in-between these chains, with an interatomic N−H distance of 2.269 Å and N−H···N angle of 158.9 °, comparison of these figures with those seen in solid ammonia (2.398 Å and 162.98 °) suggests the presence of hydrogen bonding between the two molecules (N1 and N2). Each N1 molecule is bonded in this way to 2 equidistant N2 molecules. With a minimum observed distance of 2.32 Å, the BH···HN contacts seen in $Li(NH_3)BH_4$ are not observed to the same degree here and this may be a contributing factor to the low melting point of the phase.

The openness of the structure provides an appealing explanation of its low melting point: the already well established network of ammonia molecules can easily solvate the $LiBH_4$ chains. A preliminary inspection of the refined thermal parameters suggests a great deal of disorder in the second ammonia molecule, which is less pronounced in both the ammonia molecule bonded to the lithium atom, and the borohydride unit. While it is not appropriate to report these here given the poor fit of the model to the diffraction data, the implications of disorder from the calculated data are discussed in Sections 3.4.3 and 3.4.4.

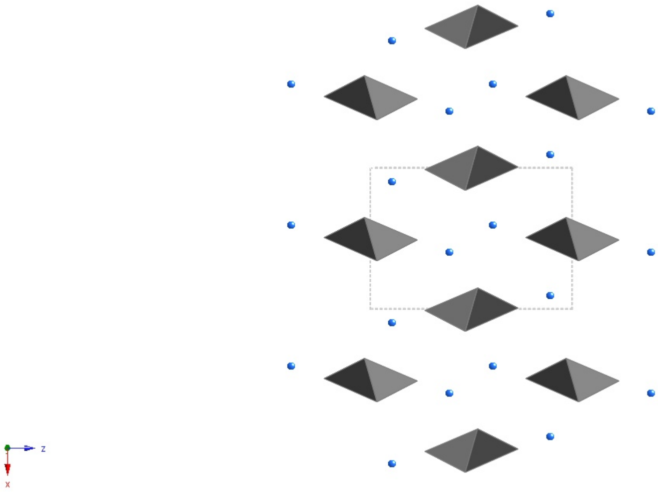

Figure 3.20: The $Li(NH_3)_2BH_4$ structure, viewed slightly off the y-axis. Hydrogen atoms are omitted for clarity, Li atoms are shown in grey, boron in brown and nitrogen in blue. $Li(NH_3)(BH_4)_3$ polyhedra are highlighted in grey.

3.4.3 Geometry-optimised Structure and Properties

The structure refined from the X-ray diffraction data was used as a starting point for DFT geometry optimisation. There was little observable change in the structure, as was the case for $Li(NH_3)BH_4$ (within a tolerance of 0.001 Å) there was no change from the *Pnma* starting symmetry. Similar bond lengths are observed before and after optimisation; with Li−B at 2.63 Å before and 2.54 Å after, and Li−N at 2.05 Å both before and after. There is a significant change in N−H···N bond length changing from 1.79 Å before to 2.27 Å after optimisation with a change in N−H···N bond angle from 167.3 ° before to 158.9 ° after. The changes in N−H···N distances are in part due to the N−H bond length being fixed to 0.90 Å during simulated annealing and allowed to vary in optimisation to reach a relaxed average of 1.03 Å.

This movement brings the calculated NH_3 bond lengths more in line with those seen in solid ammonia.

Despite problems with gathering adequate diffraction data, the similarities to $LiBH_4$ and $Li(NH_3)BH_4$, with similar bond lengths and atomic positions, strengthen the case that Section 3.4.2 details the correct structure. Furthermore, phonon calculations were carried out to check the stability of the structure. No negative modes were calculated, suggesting the structure is stable and exists in a local minima on the potential energy surface. The final calculated atomic positions are given in Table 3.5.

Table 3.5: The calculated atomic coordinates of the $Li(NH_3)_2BH_4$ structure.

atom	site	x	y	z
H	H1	0.95438	0.43705	0.76746
H	H2	0.28878	-0.02723	0.93420
H	H3	0.35456	0.56707	0.57758
H	H4	0.09767	0.25000	0.74224
Li	Li5	0.95115	0.25000	0.58476
N	N6	0.99187	0.25000	0.73097
H	H7	0.33507	0.75000	0.05704
H	H8	0.46989	0.75000	0.94421
H	H9	0.50483	0.75000	0.57812
B	B10	0.34603	0.75000	0.96803
N	N11	0.40585	0.75000	0.60666
H	H1	0.95438	0.43705	0.76746

In the results of the phonon calculation, a number of low energy NH_3 librational modes are observed. The first significant one appears at 128 cm^{-1} and involves the movement of N2. Several other low energy, N2, librational modes are observed, though none as low in energy as the some of the N1 modes seen in $Li(NH_3)BH_4$. The N1 librational modes in $Li(NH_3)_2BH_4$ are found at higher energy than in $Li(NH_3)BH_4$. In the case of the N1 modes, the higher energy is thought to be due to hydrogen bonding between N1 and N2 increasing the rotational energy barrier. Figure 3.21 shows the calculated mean squared displacement of the atoms nearest to the lithium site at 298 K. Here it can be seen that the displacement of hydrogen atoms bonded to N2 is greater than hydrogen atoms bonded to N1, which may be explained by localisation of N1 hydrogen atoms that is forced by hydrogen bonding. Comparison of the N1 ammonia molecule thermal ellipsoids with its equivalent in $Li(NH_3)BH_4$, that is shown in Figure 3.14 is striking.

The full assignment of calculated modes is given in Appendix D.3. A number of interesting features are observed in particular the coupling of N1 and N2 modes; consistently the motion of N1 coincides with the motion of N2 but not vice versa, showing the strong interaction between the two ammonia molecules. The large number of acoustic modes and N2 translational modes show that there is a large amount of ammonia mobility in this structure, and corroborates with the observation of a low melting point.

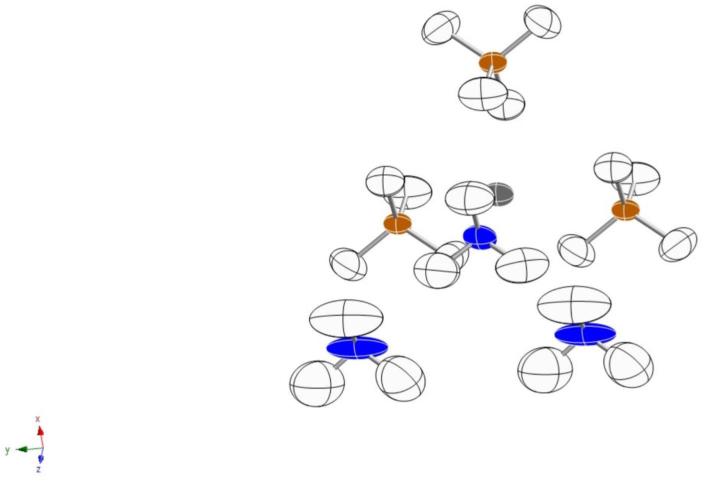

Figure 3.21: The calculated 50 % probability ditributions for the mean squared displacement of atoms at 298 K for a single $Li(NH_3)(BH_4)_3$ unit and nearest NH_3 molecules in $Li(NH_3)_2BH_4$.

3.4.4 Molecular Dynamics

The molecular dynamics calculations performed on $Li(NH_3)_2BH_4$ were identical to those for $Li(NH_3)BH_4$, discussed in Section 3.3.8, and were performed at 150 K for a time of 5.0 ps to aid direct comparison between the two structures. From observation of the movies it is clear that 1) the N2 ammonia molecule rotates quickly; 2) the N1 ammonia molecule rotates notably less frequently than the N2 molecule; and 3) BH_4^- anions do not rotate but oscillate about a fixed position (i.e. they are not disordered). Results that can be easily pictures are displayed in Figure 3.22, here it can be seen that there is significant movement of all atoms. The N2 molecules move more than other atoms and the network of ammonia molecules resulting in low melting point is clear, particularly where the 2 ammonia sites close to the centre of the unit cell are close to exchanging. A fascinating comparison of these calculations with those performed on $Li(NH_3)BH_4$ is the absence of significant atomic movement and/or migration in the y-direction. It could be that this is due to increasing separation of the $Li(NH_3)(BH_4)_3$ chains, which would suggest that those compounds with greater ammonia content will have lower ionic conductivity. If this were the case then an ammonia storage system utilising $LiBH_4$ would have a simple and direct way of monitoring ammonia content within the solid.

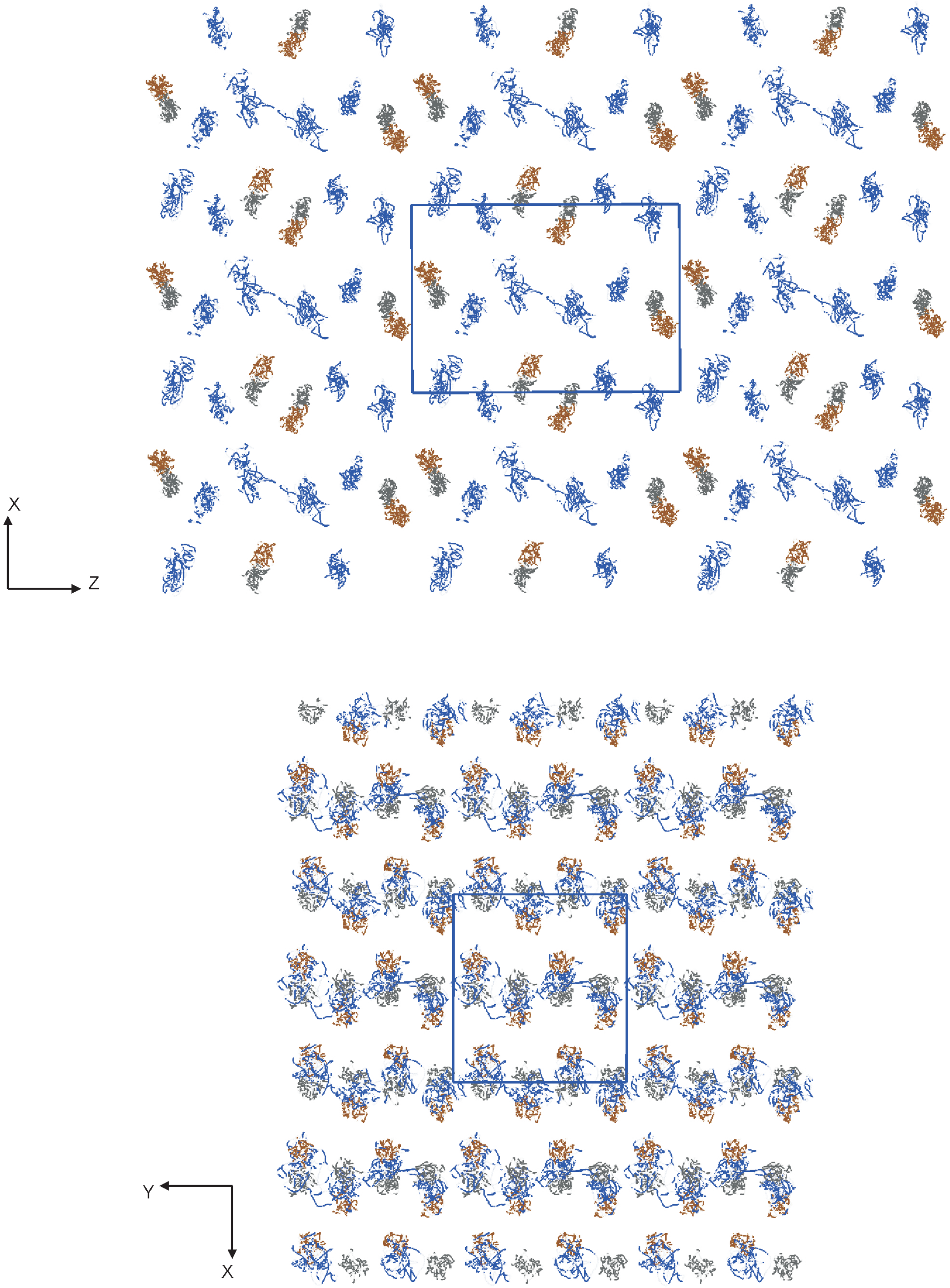

Figure 3.22: The calculated movement of Li (grey), N (blue) and B (brown) atoms in $Li(NH_3)_2BH_4$ at 150 K, with points representing atomic positions at 0.5 fs intervals over a period of 5.5 ps, viewed down the y-axis and z-axis, above and below respectively.

3.5 Lithium Borohydride Triammine

The triammine was produced and characterised in-situ using the IGA$^{\mathrm{n}}$ apparatus. The phase was isolated at room temperature using a set-point ammonia vapour pressure of 67 mbar on both GEM and HRPD. Although the HRPD data are good, a combined approach using both Rietveld refinement and DFT calculations was used in structure solution.

3.5.1 Combined Neutron Diffraction and DFT Structure Solution

Bragg peaks in the HRPD diffraction pattern were indexed to a new orthorhombic unit cell. Lattice parameters of a = 8.08499(7) Å, b = 9.81191(8) Å, c = 8.20782(7) Å and cell volume V = 651 Å^3 were refined using the Pawley method in TOPAS. Comparing the unit cell volume with that of $LiBH_4$, and assuming that Z = 4 for $Li(ND_3)_3^{11}BD_4$, it is observed that the approximate excess volume for each ND_3 molecule is (651-217)/12 Å^3 = 36 Å^3. This value is slightly small but still consistent with other ammines, so it follows that the unit cell is of reasonable size. The extracted integrated intensities from the refinement were analysed for systematic absences, the concluding reflections were; the absent (021) suggesting $Cc--$ is preferred, the present (310) suggesting $C--2_1$, $C-c-$, $Cc--$, or $Ccc-$, and the present (401) suggesting $C--2_1$, $C--(ab)$, $Cc--$, or $Cc-(ab)$. Thus the structure belongs to one of the space groups $Ccm2_1$, $Cc2m$ or $Ccmm$. It is worth noting here that in these space groups the order of the final two characters $m2_1$, $2m$ and mm is commutative and thus the y- and z- axes are interchangeable.

The structure was solved using the simulated annealing process within TOPAS. It was assumed that each lithium cation would be coordinated by three ND_3 molecules and one $^{11}BD_4^-$ anion, the preceding arrangement was described using a single rigid body in the simulated annealing process. Three ND_3 molecules and one BD_4 unit were fixed in an ideal tetrahedron about the central Li atom, the ammonia molecules were allowed to rotate freely and the BD_4 unit was allowed to tumble, whilst bond lengths were constrained to vary within the reasonable limits: 0.95 Å to 1.05 Å for N−D, 2.3 Å to 2.7 Å for Li−B, 1.5 Å to 2.5 (2.2) Å for Li−N, and 1.21 Å for B−D, the Li−N−D angle was constricted to vary within the limits 109 ° to 112 °. Through a series of a refinements, in each of the possible space groups, the occupancies of sites were also allowed to vary in order to account for the symmetry of the various space groups. A global minima was repeatedly found that placed N, Li and B atoms at (x, ca. 1/2, z), close to the mirror plane in $Ccm-$. Locating these atoms at (x, 1/2, z), further simulated annealing was performed. It was observed that of the three possible space groups, $Ccm2_1$ consistently produced the most chemically reasonable structure. Using this space group, a new rigid body was defined that accounted for placement of the boron, lithium and one nitrogen atom of the $Li(ND_3)_3BD_4$ tetrahedron on the (x, 1/2, z) mirror plane.

The neutron data show a greater reduction of intensity at low d-values than would normally be expected, it is suggested that this is due to some level of disorder within the structure. The data are also somewhat lacking, with very few intense Bragg reflections available to refine a complicated model. Despite employing a number of different models and allowing free movement of atoms, it was not possible to obtain a high quality fit of the model to the data. For these reasons DFT calculations were also employed in the structure solution.

DFT geometry optimisation was carried out using the result of the initial Rietveld refinement as a starting structure. The resultant structure is virtually indistinguishable from the starting one, with small differences in bond-lengths, Li−B was 2.28 Å before optimisation and 2.54 Å after, and Li−N were 2.19 Å and 2.20 Å before and 2.10 Å and 2.11 Å after optimisation. The calculated structure, with no change to the atomic positions and without allowing for any disorder, produced a good fit to the diffraction data with the parameters: $R_{wp} = 4.608$, $R_{exp} = 2.950$, and $\mathrm{GOF}(\chi) = 1.562$. The diffraction data, with the final fit of the Rietveld refinement of the model to the data, are shown in Figure 3.23. Final calculated atomic positions are given in Table 3.6.

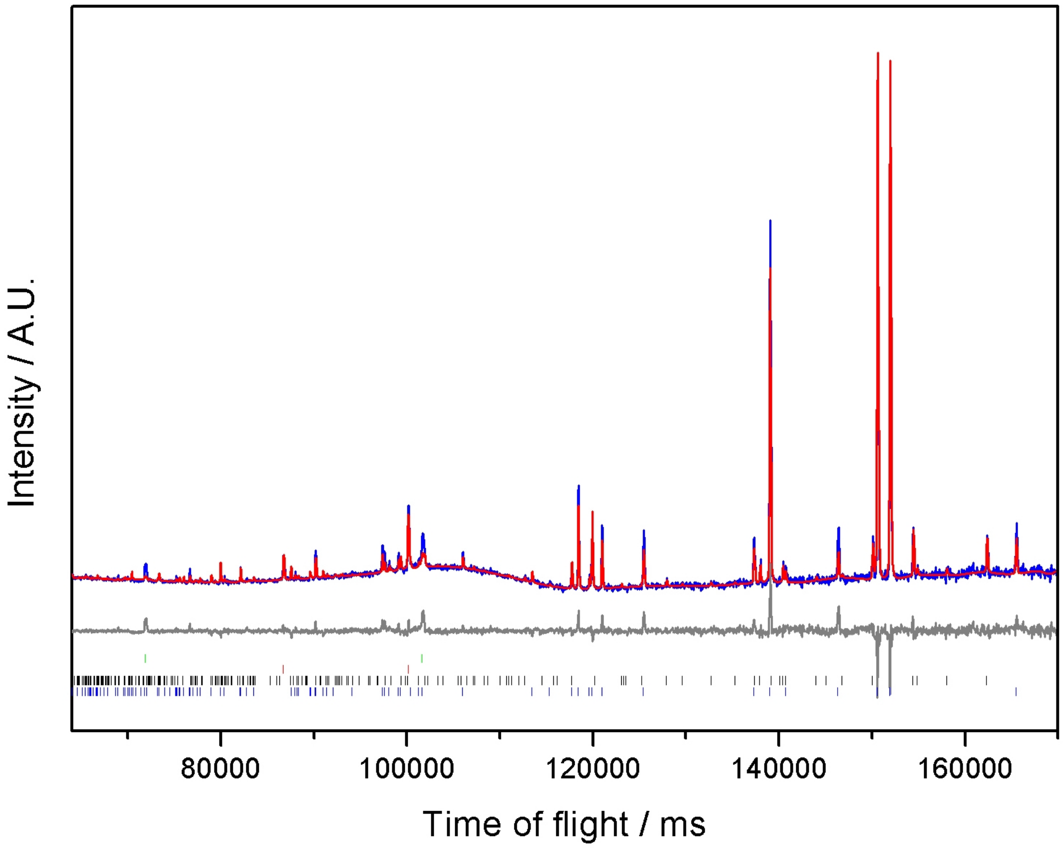

Figure 3.23: Final fit to the data for Rietveld refinement of the $Li(NH_3)_3BH_4$ model to neutron powder diffraction data collected using HRPD. Experimental data are shown in blue, calculated in red with the difference in grey, tick marks show the expected positions of Bragg reflections for (from top to bottom) V, Fe, $Li(NH_3)_4BH_4$ and $Li(NH_3)_3BH_4$.

3.5.2 Structural Description and Discussion

During structural solution it was assumed that the molecules would be arranged in $Li(NH_3)_3BH_4$ tetrahedra rather than in a more open arrangement as seen with $Li(NH_3)_2BH_4$. This assumption holds, and the final structure is reasonable, given that 1) an open structure would be likely to have a low melting point, as seen with $Li(NH_3)_2BH_4$; 2) as observed in the spectrochemical series bonding between Li^+ and

Table 3.6: The atomic coordinates from the calculation and B_{iso} from Rietveld refinement of the final $Li(NH_3)_3BH_4$ structure.

atom	site	x	y	z	B_{iso}
H	H1	-0.39768	0.25065	0.64263	9.5(0.2)
H	H2	-0.62497	0.26405	0.18701	9.5(0.2)
H	H3	-0.79524	0.44251	0.46743	9.5(0.2)
H	H4	-0.67351	0.57920	0.47421	9.5(0.2)
H	H5	-0.77535	0.54095	0.30647	9.5(0.2)
N	N6	-0.71000	0.49855	0.40178	9.5(0.2)
H	H7	-0.50000	0.14173	0.52886	9.5(0.2)
H	H8	-0.50000	0.08986	0.15318	9.5(0.2)
H	H9	-0.50000	0.23422	0.97840	9.5(0.2)
Li	Li10	-0.50000	0.37472	0.36784	9.5(0.2)
B	B11	-0.50000	0.21327	0.12573	9.5(0.2)
N	N12	-0.50000	0.24134	0.56854	9.5(0.2)

NH_3 should be stronger than bonding between Li^+ and BH_4^-; 3) while with X-ray diffraction it would be hard to see a difference between the isoelectronic NH_3 and BH_4^-, the total coherent scattering of 27.8 barn for ND_3 and 22.4 barn for $^{11}BD_4^-$ mean that the two sites should be distinguishable; and 4) the stabilisation of the structure via dihydrogen bonding should be a significant thermodynamic factor on formation of the structure, it is hard to conceive a structure with a greater number of these bonds than the one presented in Figure 3.24.

When considering the structure as part of the $Li(NH_3)_nBH_4$ group, it is convenient to view down the z-axis where it can be seen that the $Li(NH_3)_3BH_4$ tetrahedra are arranged in pairs which form rows running in the z-direction. These rows join together to form layers that run in the yz-plane and are discussed further in Section 3.7, where a clear image of the molecular structure is also shown. The BH···HN distances suggest that there is a significant number of both inter- and intra-layer dihydrogen bonds that act to stabilise the structure. The different BH···HN distances are given in Table 3.7 and reveal that the mean inter- and intra-layer bond distances are 2.29 Å and 2.34 Å respectively. Even though these distances suggest relatively weak bonds, their importance in stabilising the structure is reflected in their sheer number, as shown in Figure 3.24.

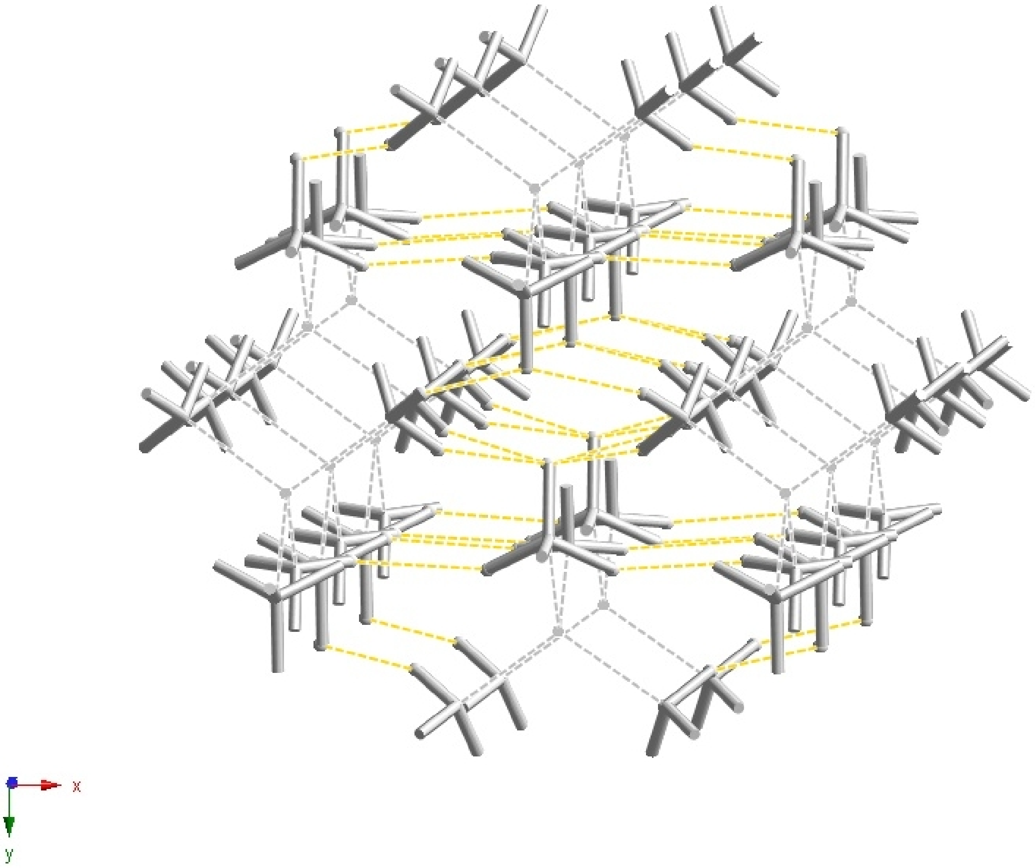

Figure 3.24: The structure of $Li(NH_3)_3BH_4$, with Li−B and Li−N bonds shown as dashed grey lines, and H···H contacts of ≤ 95 % of the Van der Waals radii (i.e. 2.28 Å) shown as dashed gold lines

Table 3.7: BH···HN distance observed in the final $Li(NH_3)_3BH_4$ structure.

Hydrogen Atom Sites	Inter- or Intra-row	Number of Bonds	Distance / Å
8–3	Inter-	2	2.27
8–5	Inter-	2	2.26
9–3	Intra-	2	2.40
9–4	Inter-	2	2.31
2–4	Inter-	1	2.36
2–1	Intra-	1	2.24

3.6 Lithium Borohydride Tetra-ammine

Lithium borohydride tetra-ammine was produced and characterised in-situ using the IGA^{n} apparatus. The phase was isolated at room temperature using a set-point ammonia vapour pressure of 1000 mbar on both GEM and HRPD, though was observed to exist with vapour pressures as low as 96 mbar. A combined approach using both Rietveld refinement and DFT calculation was once again used in the structural solution process.

3.6.1 Neutron Diffraction and DFT Structure Solution

Bragg peaks in the HRPD diffraction data were indexed to a new orthorhombic unit cell. Pawley refinements were performed using TOPAS in each of the possible orthorhombic space groups, and resulted in lattice parameters of a = 11.9345(1) Å, b = 7.06904(7) Å, c = 9.96326(8) Å, and cell volume V = 841 Å^3. Performing a check on volume and assuming that Z = 4, it can be seen that (841-217)/16 = 39 Å^3 are left for each ammonia molecule which is consistent with other ammines and thus the size of the unit cell is considered reasonable. The structures of $Li(NH_3)_4Br$ and $Li(NH_3)_4I$ have been reported,[103] and comparison between them and the cell for $Li(NH_3)_4BH_4$ is given in Table 3.8. It appears likely that the three compounds are isostructural and share the space group *Pnma*.

Table 3.8: A comparison of the unit cells of $Li(NH_3)_4Br$, $Li(NH_3)_4I$ and $Li(NH_3)_4BH_4$

	Compound		
	$Li(NH_3)_4Br$	$Li(NH_3)_4BH_4$	$Li(NH_3)_4I$
x	11.947(5)	11.9345(1)	12.646(3)
y	7.047(4)	7.06904(7)	7.302(1)
z	9.472(3)	9.96326(8)	9.790(2)
Volume	797.5	840.6	904.0
Space group	*Pnma*	*Pnma*	*Pnma*

The ideal approach to solve this structure would perhaps be to locate the heavier atoms within the cell using X-ray diffraction and then locate the hydrogen atoms using neutron diffraction data. In absence of X-ray data and given the bulk of the scattering from the cell is due to deuterium atoms, it was necessary to model the $Li(ND_3)_4$ and BD_4 tetrahedra as rigid bodies constrained to vary within sensible limits during the refinement process. As a starting point lithium and boron positions were interpolated from the lithium and halide sites in $Li(NH_3)_4Br$ and $Li(NH_3)_4I$. Fractional coordinates of the Li, ^{11}B and two of the three possible N sites were fixed in the (x, 1/4, y) mirror plane but otherwise allowed to vary freely. It was clear during the refinement process that a significant amount of disorder was present within the structure. As was the case with the $Li(NH_3)_3BH_4$ data, there is a significant drop in the intensity of Bragg peaks at low d-spacing, also the vapour pressure of < 96 mbar required to isolate the phase suggests a large amount of ammonia mobility. Disorder was modelled by increasing the number of hydrogen sites around the nitrogen atom to 6 instead of 3, conceptually representing a spinning ammonia molecule, and modelling the hydrogen sites around the boron atom, and nitrogen sites around the lithium atom as a cube. The occupancies of these disordered sites were allowed to vary freely while maintaining the appropriate Li:N, N:D and ^{11}B:D ratios. The inclusion of disorder within the model greatly improved the goodness of fit to the data, whilst taking into account the additional refineable variables. It was observed that there was disorder present in the hydrogen sites about the N and B atoms, but a single set of N sites was preferred. The best fit of the model to the data is shown in Figure 3.25, and produced the fit statistics: $R_{wp} = 3.316$, $R_{exp} = 1.876$ and $\mathrm{GOF}(\chi) = 1.768$. It was possible to achieve a better fit while only refining the model against part of the data but this approach is limited as without considering the entire pattern there is not enough data to accurately refine a disordered model. Within the disorder a site preference was shown for the ‘b’ sites of BD_4 that were occupied at 75 % and the ‘a’ sites in ND_3 that were occupied at 61 %, though why this preference is shown is not clear.

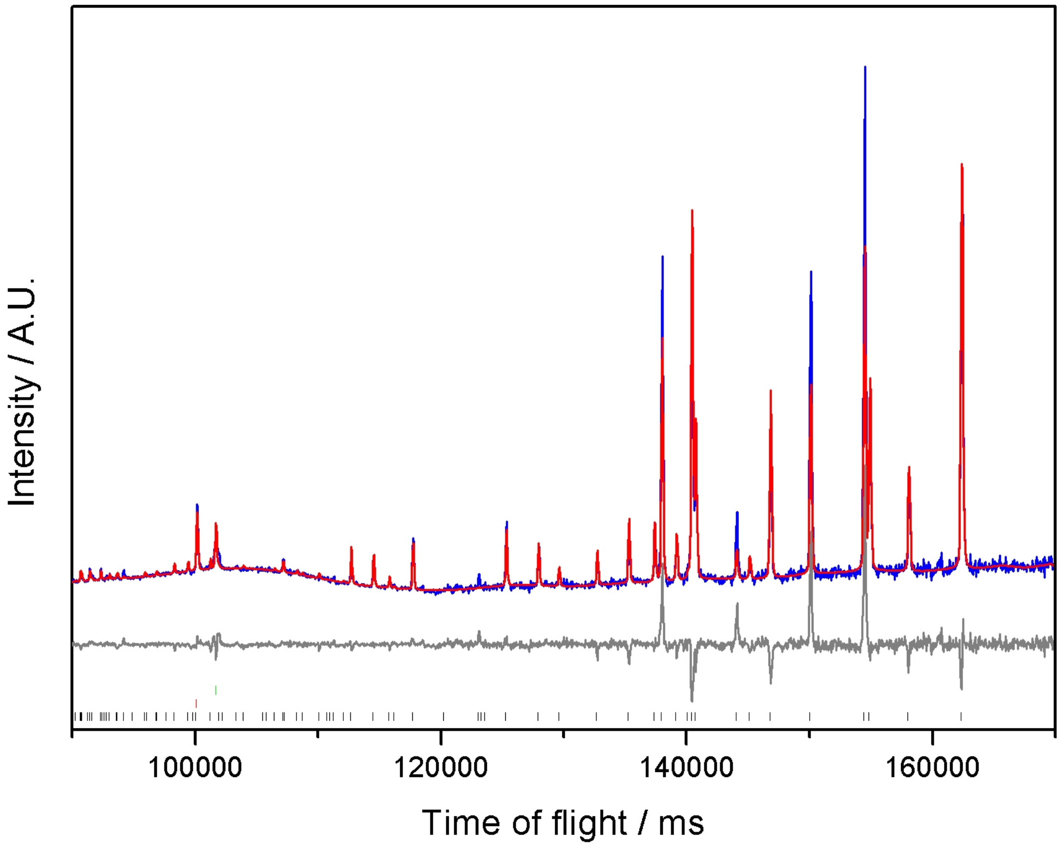

Figure 3.25: Final fit to the data for Rietveld refinement of the $Li(ND_3)_4BD_4$ model to neutron powder diffraction data collected using HRPD. Experimental data are shown in blue, calculated in red with the difference in grey, tick marks show the expected positions of Bragg reflections for V, steel and $Li(ND_3)_4BD_4$.

To confirm the structure, DFT geometry optimisation was performed using a structure that positioned the disordered hydrogen atoms on the sites with highest occupancy. The resulting structure showed a great deal of similarity with the starting one; Table 3.9 shows there was small increase in the mean bond lengths that is inline with what may be expected and discussed both in Section 2.12 and earlier in this Chapter. The biggest discrepancies in bond lengths arise for those associated with NH_3, these may be a result of significant ammonia mobility and rotational motion at room temperature. Although there are large changes in the N−Li−N bond angles, both models show irregular LiN_4 tetrahedra. The refinement of the calculated structure with fixed atomic coordinates did not provide a good fit to the data. It is proposed that the reason for this and the observed differences in bond angles is significant disorder present at room temperature. These differences are exaggerated by the fact that the calculated structure is effective at 0 K in a fixed system with no net forces acting on atoms while the experimental structure is at 298 K with a dynamic ammonia equilibrium in force. The final atomic positions from Rietveld refinement are given in Appendix E.5 and Table 3.10 gives the final calculated atomic positions. The images presented are, unless otherwise stated, produced from the calculated structure as these offer the most reasonable bond angles.

Table 3.9: A comparison of bond lengths in $Li(NH_3)_4BH_4$ before and after geometry optimisation

Bond	Length Before Optimisation / Å	Length After Optimisation / Å
Li−N	1.95	2.08
	2.02	2.10
	2.17*	2.08
Mean Li−N	2.08	2.09
B−H	1.23	1.23
N−H	0.97	1.03

3.6.2 Structural Description and Discussion

During the refinement process, ammonia molecules were fixed in tetrahedra around the Li atoms. The alternative would be to have an arrangement of $Li(NH_3)_{4\text{-}n}BH_n$ tetrahedra with n free NH_3 molecules as is seen in $Li(NH_3)_2BH_4$ though this would presumably produce a low melting point solid. It is also unlikely that the 4th ammonia molecule will be free, as this is not a feature of the $Li(NH_3)_4Br$ or $Li(NH_3)_4I$ and NH_3 is generally considered a better ligand than BH_4^- so should bond to Li^+ preferentially. Furthermore, when BH_4^- is not bonded to the Li^+ cation, it is available for an increased number of dihydrogen bonds that act to stabilise the structure.